Middle to late Miocene extremely rapid exhumation and thermal reequilibration in the Kung Co rift, southern Tibet

Jeffrey Lee,[1] Christian Hager,[2,3] Simon R. Wallis,[4] Daniel F. Stockli,[2] Martin J. Whitehouse,[5] Mutsuki Aoya,[6] and Yu Wang[7]

Received 12 May 2010; revised 7 December 2010; accepted 21 December 2010; published 18 March 2011.

[1] The Kung Co rift is an approximately NNW striking, WSW dipping normal fault exposed in southern Tibet and is part of an extensive network of active approximately NS striking normal faults exposed across the Tibetan Plateau. Detailed new and published (U-Th)/He zircon and apatite thermochronometric data from the footwall of the early Miocene Kung Co granite provide constraints on the middle Miocene to present-day exhumation history of the footwall to the Kung Co fault. Inverse modeling of thermochronometric data yield age patterns that are interpreted as indicating (1) initiation of normal fault slip at ~12–13 Ma and rapid exhumation of the footwall between ~13 and 10 Ma, (2) acceleration of normal fault slip at rates of 21.9–6.9 mm/yr at ~10 Ma, (3) rapid thermal reequilibration between 10 and 9 Ma, and (4) slow exhumation and/or quiescence from ~9 Ma to the present day. Hanging glacial valleys in the footwall and fault scarps that cut late Quaternary till and moraine deposits indicate that fault slip continues today. Middle to late Miocene initiation of extension across the Kung Co rift is broadly the same as the documented initiation of EW extension across the south central Tibetan Plateau. Eastward flow of middle or lower crust from beneath Tibet accommodated by northward underthrusting of Indian crust beneath Tibet provides a plausible explanation for the onset of EW extension across the Tibetan Plateau.

Citation: Lee, J., C. Hager, S. R. Wallis, D. F. Stockli, M. J. Whitehouse, M. Aoya, and Y. Wang (2011), Middle to late Miocene extremely rapid exhumation and thermal reequilibration in the Kung Co rift, southern Tibet, *Tectonics*, *30*, TC2007, doi:10.1029/2010TC002745.

[1]Department of Geological Sciences, Central Washington University, Ellensburg, Washington, USA.
[2]Department of Geology, University of Kansas, Lawrence, Kansas, USA.
[3]Now at Chevron U.S.A. Inc., Houston, Texas, USA.
[4]Department of Earth and Planetary Sciences, Graduate School of Environmental Studies, Nagoya University, Nagoya, Japan.
[5]Laboratory for Isotope Geology, Swedish Museum of Natural History, Stockholm, Sweden.
[6]Institute of Geology and Geoinformation, National Institute of Advanced Industrial Science and Technology, Tsukuba, Japan.
[7]Geologic Labs Center, China University of Geosciences, Beijing, China.

0278-7407/11/2010TC002745

1. Introduction

[2] The Himalayan orogeny records Eocene to Recent continental collision and convergence between India and Asia and profound crustal thickening. Yet, active deformation in the Tibetan Plateau is dominated by NS striking normal faults and kinematically linked NW and NE striking strike-slip faults. Several research groups have postulated that EW crustal extension within the Tibetan Plateau is the result of constant stress along the southern margin of the plateau, but have proposed different driving mechanisms including (1) basal shear caused by the Indian plate sliding obliquely beneath Tibet along a gently dipping, arcuate plate boundary [*McCaffrey and Nabelek*, 1998; *Liu and Yang*, 2003] and (2) lithospheric downwarping and oroclinal bending [*Klootwijk et al.*, 1985]. Alternatively, others have proposed that a change in the stress field and subsequent gravitational spreading resulted in the initiation of EW crustal extension. Postulated models include (1) removal of lithospheric mantle [*England and Houseman*, 1989; *Molnar et al.*, 1993; *Jiménez-Munt and Platt*, 2006]; (2) changes in the thermal structure and density distribution within the upper crust and mantle [*Blisniuk et al.*, 2001]; (3) flow within a low-viscosity lower crust [*Shen et al.*, 2001; *Copley and McKenzie*, 2007; *Cook and Royden*, 2008]; (4) underthrusting of Indian lithosphere beneath the southern half of Tibet [*DeCelles et al.*, 2002]; and (5) cessation of mantle upwelling and back-arc spreading along the eastern edge of Asia [*Yin*, 2010].

[3] These models make testable predictions about the spatial and temporal distribution of extensional faulting across the Tibetan Plateau. For example, oroclinal bending [*Klootwijk et al.*, 1985] predicts that extension should be restricted to southern Tibet and extension driven by underthrusting of Indian lithosphere beneath southern Tibet implies that the timing of extension across the plateau should young northward [*DeCelles et al.*, 2002].

[4] To evaluate the hypothesized mechanisms by which approximately NS striking normal faults developed within the NS convergent Himalayan orogen, the spatial and temporal distribution of extension across the Tibetan Plateau are needed critical data sets. In this paper, we describe zircon and apatite (U-Th)/He thermochronometric results collected over a vertical distance of 1065 m in the footwall of the Kung Co normal fault, south central Tibet. Inverse modeling of these and published thermochronometric data document the low-temperature cooling and exhumation history of the footwall and middle to late Miocene to present-day faulting history along the Kung Co fault. From these data, we interpret middle to late Miocene initiation of extremely rapid exhumation

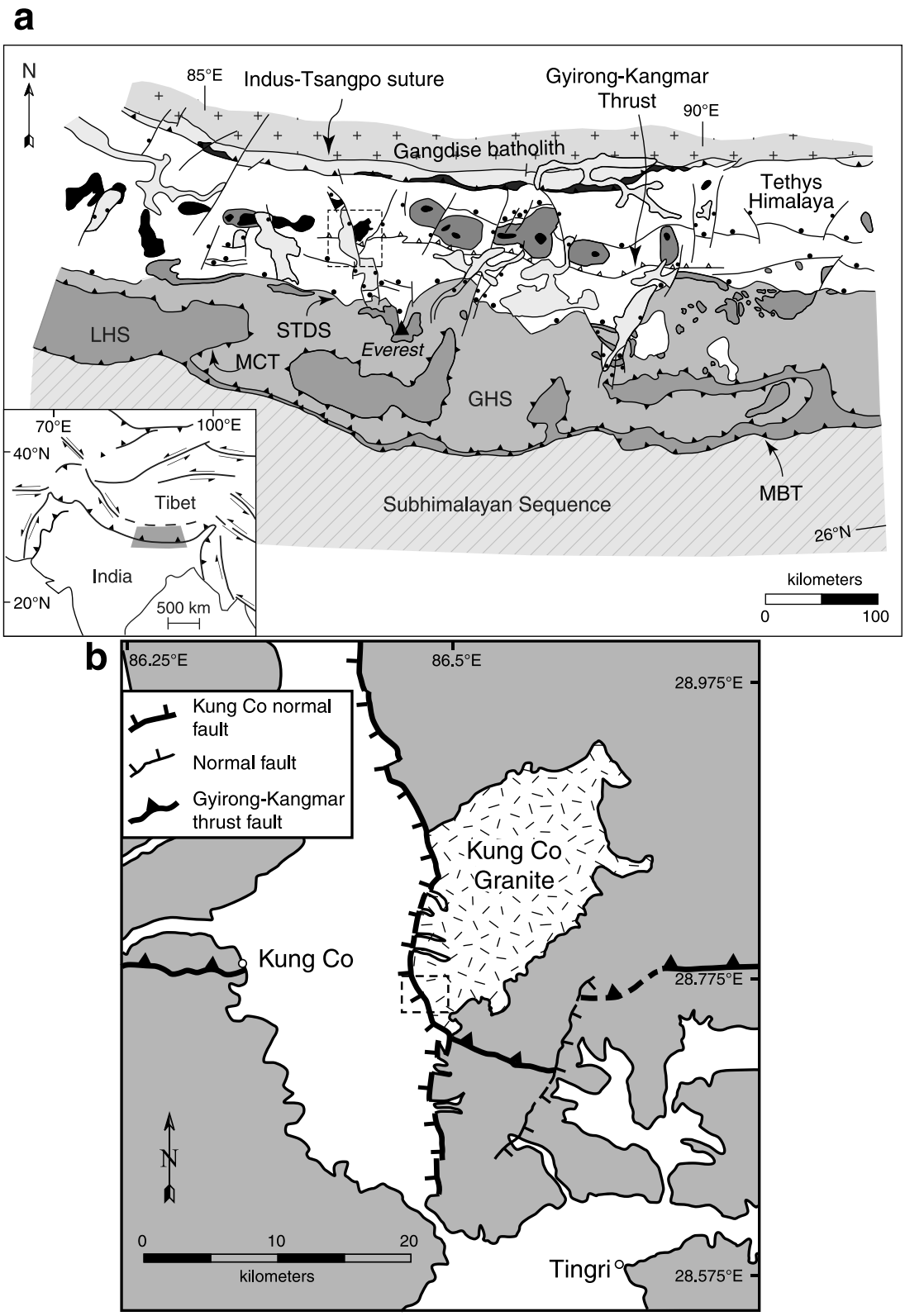
a
N
85°E
Indus-Tsangpo suture
Gyirong-Kangmar Thrust
90°E
Gangdise batholith
Tethys Himalaya
LHS
STDS
MCT
Everest
GHS
MBT
Subhimalayan Sequence
26°N
kilometers
0
100
70°E
100°E
40°N
Tibet
India
20°N
500 km
b
86.25°E
86.5°E
28.975°E
Kung Co normal fault
Normal fault
Gyirong-Kangmar thrust fault
Kung Co Granite
Kung Co
28.775°E
N
0
10
20
kilometers
Tingri
28.575°E

Figure 1

Figure 2. Oblique view east at a well-developed triangular facet, Butra Ree, along the central part of the SW dipping Kung Co fault. The fault is exposed at the base of the SW dipping planar exposure of Kung Co granite and juxtaposes till and alluvial deposits and moraines in the hanging wall against the Kung Co granite in the footwall. Height of this footwall escarpment above the valley floor is ~1.6 km. Zircon and apatite (U-Th)/He samples were collected from this triangular facet (see Figure 3 for sample locations).

along the Kung Co fault. These data, combined with timing of EW extension across the plateau, provide insight into the processes that drove the onset of extension across the Tibetan Plateau.

2. Geologic Setting

[5] The Kung Co half graben is developed within the Tethys Himalaya ~100 km northwest of Mount Everest (Figure 1). The Kung Co half graben is bounded along its east edge by the Kung Co fault, a NNW striking, WSW dipping normal fault. The fault juxtaposes a hanging wall of till and alluvial deposits, and moraines [*Armijo et al.*, 1986] upon a footwall of a weakly to moderately deformed two-mica potassium feldspar porphyritic to equigranular Kung Co granite which has intruded and contact metamorphosed strongly deformed Tethyan sediments (Figures 1, 2, and 3). Temperature-pressure conditions during contact metamorphism have been estimated at ~520°C–545°C and <3 kbar [*Mahéo et al.*, 2007, hereafter M07], implying that the Kung Co granite was emplaced at relatively shallow structural levels.

[6] The footwall of the Kung Co fault is one of several domal structures, called the North Himalayan gneiss domes, that are exposed within the Tethys Himalaya about halfway between the Indus-Tsangpo suture to the north and the High Himalaya to the south, and within the hanging wall of the north dipping Gyirong-Kangmar thrust fault (Figure 1).

3. Kung Co Fault and Associated Structures

[7] The Kung Co fault consists of a main strand defined by a fault plane that cuts a weakly foliated Kung Co granite and strongly deformed Tethyan sediments. The main strand of the fault is locally exposed within the granite and defined by polished and striated fault surfaces, fault breccias, and a set of fractures, subparallel to the fault plane, developed over a several meter wide zone in the footwall (Figure 2). The dip of the exposed bedrock fault plane ranges from 46° to 78° to the southwest; the average orientation is a dip of 60° toward

Figure 1. (a) Regional tectonic map of the south central Himalayan orogen. Major geologic features include the Main Boundary Thrust (MBT), Main Central Thrust (MCT), Greater Himalayan Sequence (GHS), Lesser Himalayan Sequence (LHS), South Tibetan Detachment System (STDS), and the North Himalayan gneiss domes which expose leucogranites (black) and high- and low-grade metamorphic rocks (dark gray) within the Tethys Himalaya. Inset map shows the location of the regional tectonic map. (b) Simplified geologic map in the region of the Kung Co rift (modified from M07). Location shown by dashed box in Figure 1a. Tethys Himalaya shown in gray. Dashed box shows location of (U-Th)/He sample map shown in Figure 3.

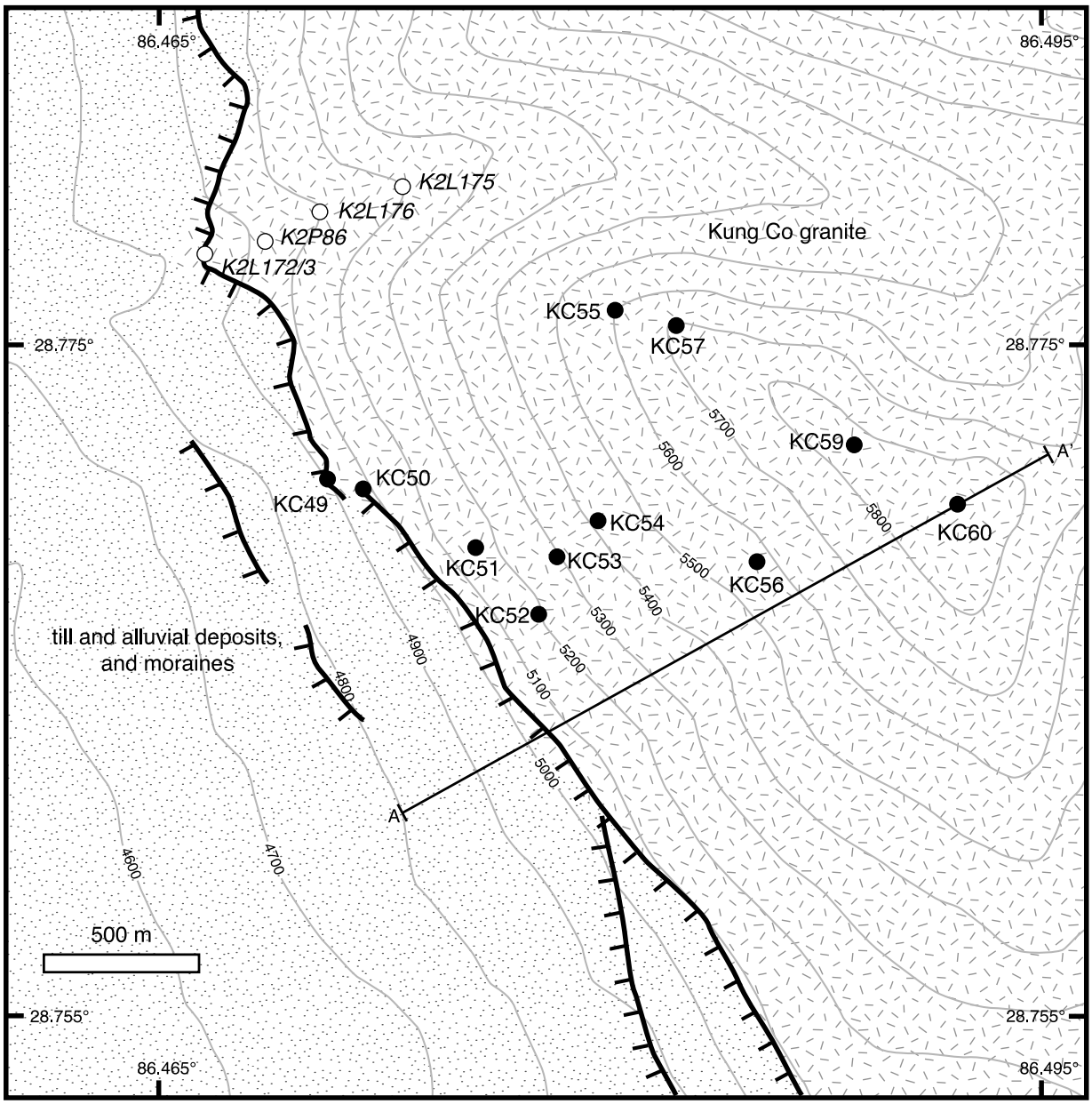

Figure 3. Simplified geologic map across the Butra Ree portion of the Kung Co rift showing location of (U-Th)/He thermochronometric samples from this study (black circles and roman font) and M07 (white circles and italic font). Location of map is shown in Figure 1b.

241° (Figure 4). Fault striations, defined by centimeter- to millimeter-spaced mullions and grooves, show a moderate range in orientation and average a trend and plunge of 226°, 59°, implying nearly pure dip slip motion (Figure 4). Using the fault kinematic analysis method of *Marrett and Allmendinger* [1990], fault slip data from the Kung Co fault yield a shallowly plunging southwest-northeast extension direction (azimuth of 235° and plunge of 15°) (Figure 4). Fractures within the granite are somewhat steeper than the fault plane with an average orientation of a 70° dip toward 235°.

[8] Secondary fault strands are exposed in the hanging wall of the primary fault, and are defined by fault scarps that cut and offset till and moraine deposits. Evidence for active faulting along the Kung Co fault includes a steep range front (~30°), well-developed triangular facets with relief as much as ~1100 m (Figures 2 and 3), hanging glacial valleys in the footwall, and fault scarps cutting late Quaternary till and moraine deposits.

[9] A weakly to moderately developed foliation defined by alignment of micas at the mesoscopic scale within the granite is cut by the Kung Co fault. Average orientation of this

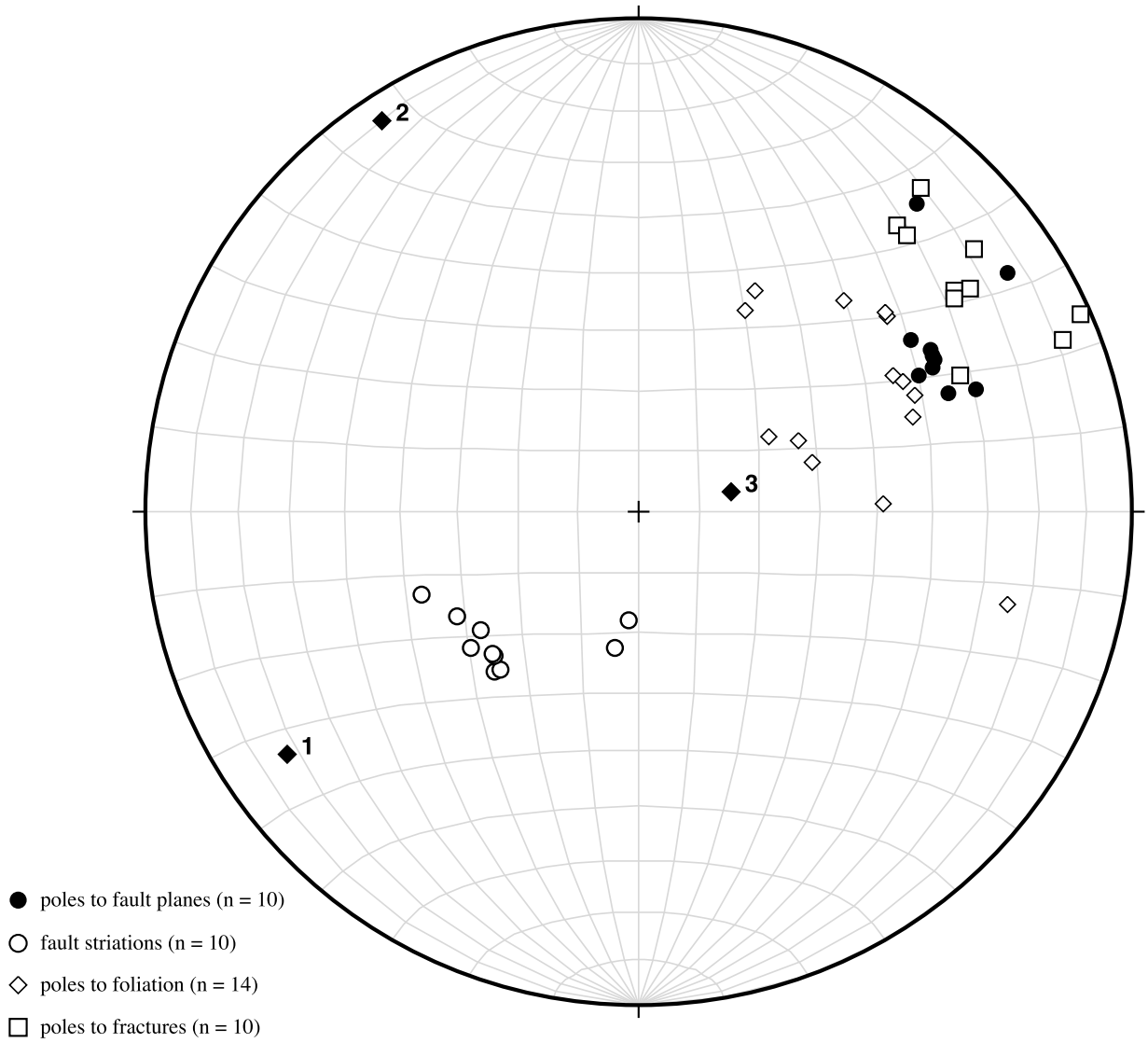

Figure 4. Lower hemisphere, equal area stereonet plot of fault planes and striations along the Kung Co fault, foliation and fractures in the Kung Co granite, and kinematic axes (solid diamonds) for fault/striation data pairs. Numbers are as follows: 1, extension axis; 2, intermediate axis; 3, shortening axis.

foliation is a 43° dip toward 242°, a bit shallower than the fault plane (Figure 4). In thin section, evidence for ductile deformation in the granite is weak. Quartz grains show subgrain development with bulging boundaries and local development of ribbon grains. Potassium feldspar grains exhibit undulatory extinction locally, but generally do not exhibit evidence for ductile deformation. Plagioclase grains show strong undulose extinction locally and are associated with fine-grained domains probably reflecting grain size reduction. These mineral textures suggest deformation temperatures of ~300°C–400°C during formation of this foliation [*Hirth and Tullis*, 1992; *Stipp et al.*, 2002; *Pryer*, 1993].

[10] The similarity in orientation of the foliation, fault plane, and fractures developed within the granite suggests that these structures record a history of progressive exhumation during normal faulting from a depth where temperatures were sufficiently high that the granite underwent weak ductile deformation to shallow crustal levels where brittle deformation dominated.

4. U/Pb Zircon Ion Microprobe Geochronology

[11] To determine the age of the Kung Co granite across which we collected a number of samples for (U-Th)/He thermochronometry, we performed U/Pb analyses of zircons from one of those samples (KD57) using a Cameca IMS1270 high mass resolution, high-sensitivity instrument. Sample locations, representative cathodoluminescence (CL) images, and concordia diagram are shown in Figures 3 and 5. Analytical techniques follow those of *Lee and Whitehouse* [2007] and results of U-Th-Pb isotopic analyses are given in Table 1.

[12] CL images of zircons from sample KD57 show bright, low (relative to rims; see below) U (1127 ppm on average)

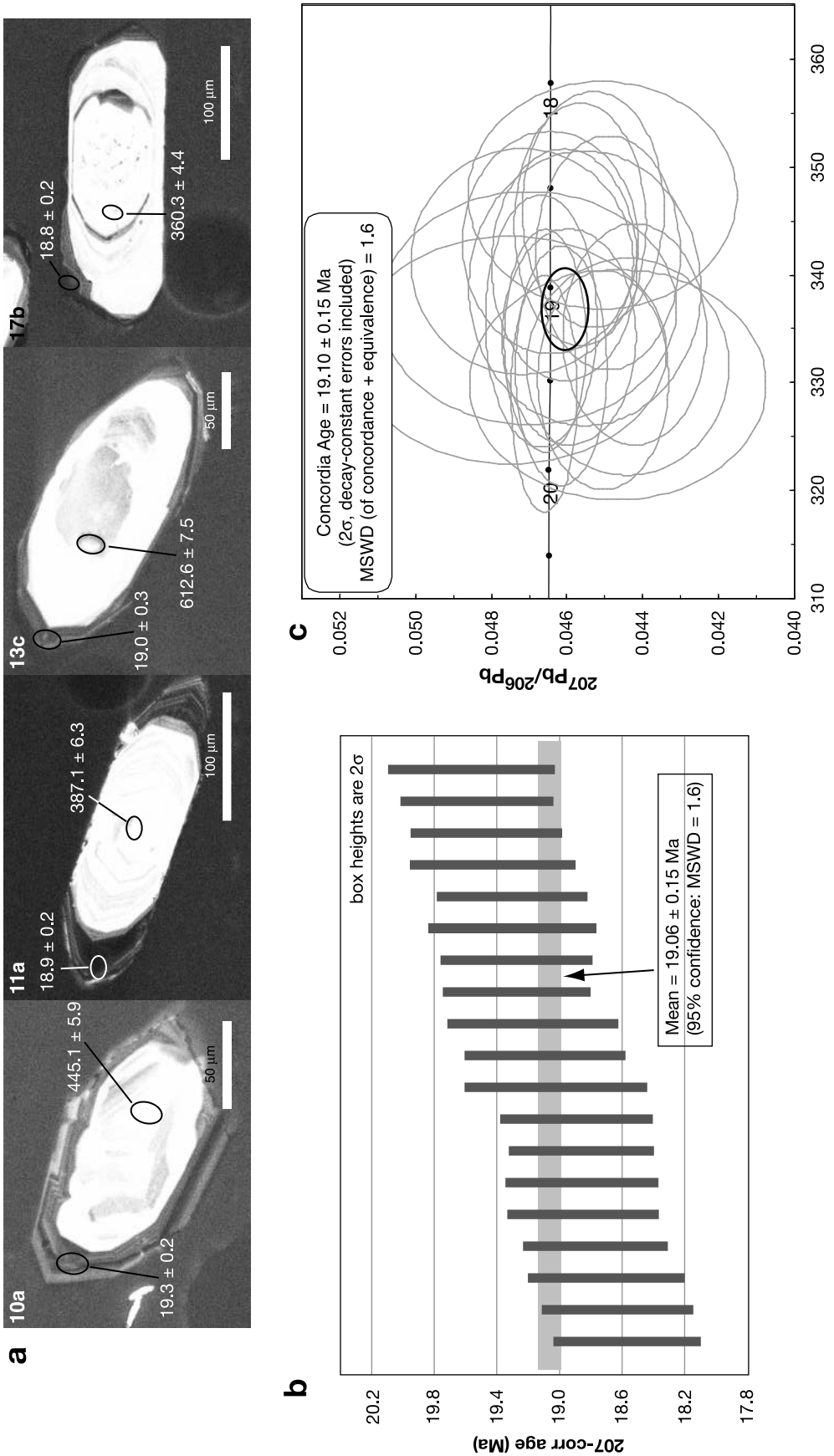

Figure 5. (a) Representative cathodoluminescence (CL) images of zircons from sample KC57. Images show analyzed spots and corresponding 207-corrected ages (±1σ). (b) Weighted average of 207-corrected ages from sample KC57. (c) Inverse concordia plot of zircon rim data (all error symbols shown at 2σ level) from sample KC57. MSWD, mean square of weighted deviates.

Table 1. Ion Microprobe U-Th-Pb Data[a]

Sample ID[b]	(U) (ppm)	(Pb) (ppm)	Th/U[c]	f_{206}[d] (%)	$^{207}Pb/^{206}Pb$ Corrected[e]	$^{207}Pb/^{206}Pb$ Uncorrected	$^{206}Pb/^{238}U$ Corrected[e]	$^{206}Pb/^{238}U$ Uncorrected	$^{207}Pb/^{206}Pb$ Age ± σ[f] (Ma)	$^{206}Pb/^{238}U$ Age ± σ (Ma)	207-Corr Age ± σ[g] (Ma)
n2702-5A-r	3,700	10	0.0078	2.05	0.0424 ± 5.7%	0.05865 ± 1.4%	0.002701 ± 1.3%	0.002757 ± 1.3%		17.4 ± 0.2	17.5 ± 0.2
n2702-29B-r	6,600	22	0.018	12.72	0.030 ± 100%	0.132 ± 12%	0.002704 ± 3.3%	0.003099 ± 2.0%		17.4 ± 0.6	17.8 ± 0.6
n2702-25B-r	3,700	10	0.0085	0.25	0.0443 ± 2.3%	0.04627 ± 1.6%	0.002757 ± 1.3%	0.002764 ± 1.3%		17.8 ± 0.2	17.8 ± 0.2
n2702-26A-r	5,400	16	0.013	0.18	0.04610 ± 1.6%	0.04756 ± 1.3%	0.002774 ± 1.2%	0.002779 ± 1.2%		17.9 ± 0.2	17.9 ± 0.2
n2702-16A-r	7,700	23	0.014	0.56	0.0464 ± 2.4%	0.05086 ± 1.8%	0.002779 ± 1.3%	0.002795 ± 1.3%		17.9 ± 0.2	17.9 ± 0.2
n2702-1B-r	5,100	15	0.017	0.16	0.04545 ± 1.6%	0.04668 ± 1.3%	0.002780 ± 1.3%	0.002785 ± 1.3%		17.9 ± 0.2	17.9 ± 0.2
n2702-7B-r	6,800	20	0.012	1.15	0.0451 ± 2.8%	0.05419 ± 1.5%	0.002789 ± 1.3%	0.002821 ± 1.3%		18.0 ± 0.2	18.0 ± 0.2
n2702-12A-r	9,300	27	0.0013	0.24	0.04540 ± 1.3%	0.04726 ± 1.0%	0.002803 ± 1.3%	0.002809 ± 1.3%		18.0 ± 0.2	18.1 ± 0.2
n2702-22B-r	8,300	25	0.041	0.2	0.04567 ± 1.3%	0.04727 ± 1.1%	0.002836 ± 1.3%	0.002842 ± 1.3%		18.3 ± 0.2	18.3 ± 0.2
n2702-28A-r	5,200	16	0.036	0.4	0.0442 ± 2.7%	0.04735 ± 1.9%	0.002861 ± 1.2%	0.002873 ± 1.2%		18.4 ± 0.2	18.5 ± 0.2
n2702-24A-r	7,900	27	0.13	0.68	0.0458 ± 2.5%	0.05119 ± 1.6%	0.002876 ± 1.3%	0.002895 ± 1.3%		18.5 ± 0.2	18.5 ± 0.2
n2702-3B-r	5,900	18	0.017	1.38	0.0451 ± 3.2%	0.05598 ± 1.2%	0.002878 ± 1.2%	0.002919 ± 1.2%		18.5 ± 0.2	**18.6 ± 0.2**
n2702-7A-r	6,100	18	0.011	0.23	0.04531 ± 1.7%	0.04714 ± 1.3%	0.002890 ± 1.3%	0.002896 ± 1.3%		18.6 ± 0.2	**18.6 ± 0.2**
n2702-8A-r	8,400	26	0.0094	0.18	0.04565 ± 1.6%	0.04705 ± 1.4%	0.002901 ± 1.3%	0.002907 ± 1.3%		18.7 ± 0.2	**18.7 ± 0.2**
n2702-29A-r	6,200	19	0.018	0.61	0.04644 ± 2.0%	0.05122 ± 1.2%	0.002915 ± 1.2%	0.002933 ± 1.2%		18.8 ± 0.2	**18.8 ± 0.2**
n2702-17B-r	8,900	27	0.0078	0.98	0.0472 ± 2.5%	0.05490 ± 1.4%	0.002930 ± 1.3%	0.002959 ± 1.3%		18.9 ± 0.2	**18.8 ± 0.2**
n2702-11A-r	6,900	21	0.024	0.29	0.04492 ± 1.7%	0.04718 ± 1.2%	0.002924 ± 1.3%	0.002932 ± 1.3%		18.8 ± 0.2	**18.9 ± 0.2**
n2702-19A-r	9,400	29	0.018	0.34	0.04424 ± 1.4%	0.04691 ± 1.0%	0.002921 ± 1.2%	0.002931 ± 1.2%		18.8 ± 0.2	**18.9 ± 0.2**
n2702-2A-r	9,500	29	0.01	0.35	0.04607 ± 1.7%	0.04886 ± 1.1%	0.002933 ± 1.3%	0.002943 ± 1.3%		18.9 ± 0.2	**18.9 ± 0.2**
n2702-13c-r	7,100	28	0.43	0.78	0.0455 ± 2.7%	0.05172 ± 1.5%	0.002952 ± 1.5%	0.002975 ± 1.5%		19.0 ± 0.3	**19.0 ± 0.3**
n2702-5c-r	7,000	24	0.11	1.64	0.0470 ± 3.4%	0.05995 ± 1.1%	0.002968 ± 1.3%	0.003017 ± 1.3%		19.1 ± 0.2	**19.1 ± 0.3**
n2702-13B-r	1,500	46	0.036	0.27	0.04668 ± 1.3%	0.04881 ± 1.0%	0.002979 ± 1.4%	0.002987 ± 1.4%		19.2 ± 0.3	**19.2 ± 0.3**
n2702-20A-r	8,200	26	0.034	0.41	0.04595 ± 1.6%	0.04923 ± 1.1%	0.002992 ± 1.2%	0.003004 ± 1.2%		19.3 ± 0.2	**19.3 ± 0.2**
n2702-9A-r	13,000	40	0.0045	0.09	0.04657 ± 0.95%	0.04730 ± 0.87%	0.002995 ± 1.3%	0.002998 ± 1.3%		19.3 ± 0.2	**19.3 ± 0.2**
n2702-17A-r	9,900	31	0.0043	3.57	0.0475 ± 3.5%	0.07565 ± 1.1%	0.003003 ± 1.3%	0.003114 ± 1.3%		19.3 ± 0.3	**19.3 ± 0.3**
n2702-10A-r	9,000	32	0.2	0.67	0.04422 ± 1.8%	0.04954 ± 0.99%	0.002990 ± 1.3%	0.003010 ± 1.3%		19.2 ± 0.2	**19.3 ± 0.2**
n2702-9B-r	6,400	20	0.2	0.91	0.0444 ± 2.5%	0.05163 ± 1.2%	0.003017 ± 1.2%	0.003044 ± 1.2%		19.4 ± 0.2	**19.5 ± 0.2**
n2702-14A-r	7,300	23	0.014	0.23	0.04504 ± 1.6%	0.04688 ± 1.1%	0.003028 ± 1.3%	0.003035 ± 1.3%		19.5 ± 0.2	**19.5 ± 0.2**
n2702-6A-r	17,000	54	0.0016	0.07	0.04660 ± 0.77%	0.04716 ± 0.70%	0.003040 ± 1.4%	0.003042 ± 1.4%		19.6 ± 0.3	**19.6 ± 0.3**
n2702-10B-r	8,400	29	0.086	0.65	0.04639 ± 1.7%	0.05155 ± 1.0%	0.003095 ± 1.3%	0.003115 ± 1.3%		19.9 ± 0.3	19.9 ± 0.3
n2702-1A-r	14,000	49	0.11	15.32	0.048 ± 22%	0.1684 ± 3.9%	0.003117 ± 1.3%	0.003681 ± 1.3%		20.1 ± 0.3	20.0 ± 0.6
n2702-13A-r	1,300	44	0.023	0.07	0.04636 ± 0.91%	0.04695 ± 0.84%	0.003256 ± 1.3%	0.003259 ± 1.3%		21.0 ± 0.3	21.0 ± 0.3
n2702-14A-i	140	0	0.0054	4.55	0.0380 ± 33%	0.0742 ± 7.5%	0.003535 ± 2.1%	0.003703 ± 1.8%		22.7 ± 0.5	23.0 ± 0.5
n2702-5A-i	1,800	7.2	0.021	(0.17)	n/a	0.04851 ± 2.0%	n/a	0.003744 ± 1.2%		24.1 ± 0.3	24.0 ± 0.3
n2702-17c-c	3,500	16	0.019	(0.11)	n/a	0.04714 ± 1.3%	n/a	0.004284 ± 1.2%		27.6 ± 0.3	27.5 ± 0.3
n2702-7A-c	13,000	247	0.017	0.41	0.0520 ± 2.2%	0.05523 ± 0.67%	0.01825 ± 4.2%	0.01833 ± 4.2%	286 ± 50	117 ± 5	116 ± 5
n2702-9B-c	610	16	0.16	(0.11)	n/a	0.05699 ± 1.3%	n/a	0.02300 ± 1.2%	491 ± 29	147 ± 2	145 ± 2
n2702-2B-i	670	26	0.032	0.1	0.0547 ± 2.0	0.0555 ± 1.9%	0.03680 ± 2.2%	0.03683 ± 2.2%	401 ± 45	233 ± 5	232 ± 5
n2702-20B-i	690	29	0.029	(0.06)	n/a	0.05777 ± 1.5%	n/a	0.03979 ± 2.2%	521 ± 33	252 ± 5	249 ± 5
n2702-24A-i	470	24	0.049	(0.03)	n/a	0.05850 ± 1.1%	n/a	0.04687 ±1.8%	549 ± 23	295 ± 5	293 ± 5
n2702-26A-c	170	10	0.29	0.26	0.0574 ± 1.9	0.05936 ± 1.5%	0.0524 ± 2.3%	0.0526 ± 2.3%	506 ± 40	329 ± 7	328 ± 8
n2702-20A-i	600	36	0.05	0.06	0.05571 ± 1.2	0.05620 ± 1.1%	0.0563 ± 1.8%	0.0564 ± 1.8%	441 ± 25	353 ± 6	352 ± 6
n2702-17B-c	800	50	0.078	0.07	0.05589 ± 0.74	0.05645 ± 0.69%	0.05765 ± 1.2%	0.05769 ± 1.2%	448 ± 16	361 ± 4	360 ± 4
n2702-11A-c	190	15	0.6	0.22	0.05617 ± 1.6	0.05785 ± 1.3%	0.0620 ± 1.7%	0.0622 ± 1.7%	459 ± 34	388 ± 6	387 ± 6
n2702-6A-i	270	18	0.11	(0.11)	n/a	0.0571 ± 2.3%	n/a	0.0624 ± 2.5%	494 ± 51	390 ± 9	389 ± 9
n2702-6A-c	590	51	0.63	(0.04)	n/a	0.05761 ± 0.72%	n/a	0.06823 ± 1.3%	515 ± 16	426 ± 5	424 ± 5
n2702-10A-c	140	13	0.91	0.34	0.0571 ± 1.9	0.05979 ± 1.4%	0.07160 ± 1.4%	0.07185 ± 1.3%	497 ± 42	446 ± 6	445 ± 6
n2702-13B-c	200	17	0.18	0.14	0.05759 ± 1.3	0.05871 ± 1.2%	0.07543 ± 1.2%	0.07554 ± 1.2%	514 ± 29	469 ± 6	468 ± 6
n2702-5B-i	510	42	0.042	(0.04)	n/a	0.05620 ± 0.75%	n/a	0.07600 ± 1.2%	460 ± 17	472 ± 6	472 ± 6
n2702-14A-c	340	29	0.18	0.11	0.05613 ± 1.5	0.05701 ± 1.4%	0.07709 ± 1.2%	0.07718 ± 1.2%	457 ± 33	479 ± 6	479 ± 6
n2702-9A-c1	500	44	0.17	0.05	0.05737 ± 0.84	0.05775 ± 0.80%	0.07854 ± 1.2%	0.07858 ± 1.2%	506 ± 18	487 ± 6	487 ± 6
n2702-3B-c	1,100	130	1.2	(0.01)	n/a	0.05678 ± 0.49%	n/a	0.0799 ± 1.4%	483 ± 11	496 ± 7	496 ± 7
n2702-5A-c	1,000	86	0.041	0.03	0.05707 ± 0.80	0.05727 ± 0.79%	0.08050 ± 1.2%	0.080520 ± 1.2%	494 ± 17	499 ± 6	499 ± 6
n2702-2A-c	610	55	0.19	0.06	0.05725 ± 0.69	0.05773 ± 0.65%	0.0811 ± 1.3%	0.0811 ± 1.3%	501 ± 15	502 ± 6	502 ± 6
n2702-5B-c	490	45	0.25	(0.03)	n/a	0.05631 ± 0.71%	n/a	0.08120 ± 1.2%	464 ± 16	503 ± 6	504 ± 6
n2702-12A-c	540	56	0.7	0.06	0.05614 ± 0.96	0.05658 ± 0.92%	0.0816 ± 1.3%	0.0817 ± 1.3%	458 ± 21	506 ± 6	507 ± 6
n2702-16A-c	580	52	0.13	0.12	0.05616 ± 0.82	0.05706 ± 0.72%	0.0821 ± 1.2%	0.0822 ± 1.2%	459 ± 18	508 ± 6	509 ± 6
n2702-13A-c	400	38	0.28	0.07	0.05519 ± 0.93	0.05576 ± 0.88%	0.0833 ± 1.5%	0.0833 ± 1.5%	420 ± 21	516 ± 7	517 ± 8
n2702-1A-c	370	37	0.2	(0.03)	n/a	0.06115 ± 0.91%	n/a	0.0867 ± 1.8%	644 ± 19	536 ± 9	534 ± 9
n2702-13c-c	1,300	150	0.51	0.05	0.06343 ± 0.54	0.06379 ± 0.52%	0.1001 ± 1.3%	0.1002 ± 1.3%	723 ± 11	615 ± 7	613 ± 8
n2702-17A-c	54	7.8	0.79	0.55	0.0641 ± 3.0	0.0684 ± 2.0%	0.1122 ± 1.2%	0.1129 ± 1.2%	747 ± 61	686 ± 8	684 ± 8
n2702-8A-c	2,100	290	0.21	0.01	0.06659 ± 0.28	0.06669 ± 0.28%	0.1208 ±1.5%	0.1209 ± 1.5%	825 ± 6	735 ± 11	733 ± 11
n2702-5c-c	110	17	0.63	(0.10)	n/a	0.06776 ± 1.3%	n/a	0.1215 ± 1.4%	861 ± 26	739 ± 9	736 ± 10
n2702-7B-c	890	160	0.83	0.06	0.06752 ± 0.41	0.06795 ± 0.40%	0.1355 ± 1.4%	0.1355 ± 1.4%	854 ± 9	819 ± 11	818 ± 11
n2702-25A-c	1,000	200	0.48	0.04	0.07093 ± 0.36	0.07119 ± 0.35%	0.1653 ± 1.4%	0.1653 ± 1.4%	955 ± 7	986 ± 13	987 ± 13
n2702-11B-c	290	91	0.63	0.03	0.09090 ± 0.75	0.09110 ± 0.74%	0.2466 ± 1.2%	0.2466 ± 1.2%	1445 ± 14	1421 ± 16	
n2702-1B-c	580	270	0.38	(0.01)	n/a	0.17708 ± 0.46%	n/a	0.3594 ± 1.2%	2626 ± 8	1980 ± 21	
n2702-10B-c	310	180	0.65	0.01	0.18271 ± 0.40	0.18281 ± 0.40%	0.4290 ± 1.3%	0.4290 ± 1.3%	2678 ± 7	2301 ± 25	

cores that exhibit oscillatory to convolute zoning to homogeneous textures (Figure 5a). Cores show a wide range in ages from ~116 to >1200 Ma, and preserved oscillatory zoning and high Th/U ratios (most analyses yield ratios >0.1) suggest these are igneous in origin and xenocrystic [e.g., *Vavra et al.*, 1999; *Rubatto and Gebauer*, 2000]. In sharp contrast to the cores are darker, oscillatory-zoned rims (Figure 5a) with very high U concentrations from ~4000 to >17,000 ppm (average 8566 ppm), accompanied mostly by very low Th/U ratios (<0.04), the few exceptions possibly represent analyses that sampled small monazite inclusions. U-Pb ages (207-corrected ages derived by projecting through the common Pb uncorrected data points onto concordia, assuming concordance) for the rims range from 20.0 ± 1.2 to 17.5 ± 0.4 Ma and a simple weighted average of all analyses yields 18.74 ± 0.21 Ma (2 sigma) but with an MSWD value of 5.7 indicating scatter beyond that explained by the observed analytical errors alone. Two possibilities (at least) may account for the spread in individual ages, either (1) variable amounts of Pb loss from very high-U zircon resulting in younger ages or (2) a U/Pb ratio calibration bias commonly documented in SIMS analysis of high-U zircons [e.g., *McLaren et al.*, 1994] that results in older ages, or a combination of both. Unfortunately, neither explanation is satisfactorily supported by the observed data: the youngest ages are observed in the lowest U zircon rims which would be least expected to undergo Pb loss and, although five analyses with >10,000 ppm U yield ages in excess of 19.2 Ma, those between 6000 and 10,000 ppm exhibit almost the entire range of rim ages. Our preferred age is based on a group of 19 rims chosen to minimize the observed MSWD from the maximum number of included analyses. These yield a weighted average 207-corrected age of 19.06 ± 0.15 Ma (2-sigma) with an MSWD of 1.6 and an almost identical Concordia age (in the sense of *Ludwig* [1998]) (Figures 5b and 5c), which we interpret as an emplacement age for the granite. Our zircon U/Pb age is more tightly constrained, but the same, within error, as the interpreted concordia lower intercept age of 22 ± 2.7 Ma from zircons analyzed using ID-TIMS (M07).

5. (U-Th)/He Thermochronometry and Inverse Modeling

[13] To gain insight into the low-temperature cooling and exhumation history of the footwall related to slip along the Kung Co normal fault, we collected 11 samples for zircon and apatite (U-Th)/He thermochronometry from the Kung Co granite along an ~1065 m high vertical transect up Butra Ree, a well-developed triangular facet exposed along the southern trace of the fault (Figures 2, 3, and 6). Zircon and apatite (U-Th)/He sample processing and analytical procedures for samples from this study follow that described by *Lee et al.* [2009] and zircon and apatite (U-Th)/He age results are given in Table 2.

[14] (U-Th)/He zircon and apatite ages from our transect yield an elevation invariant weighted mean age of 10.0 ± 2.6 Ma (Figure 7). There is no significant difference in age among apatite-zircon pairs for any of the samples, indicating very rapid exhumation. M07 reported (U-Th)/He zircon and apatite ages for five samples collected along an ~675 m horizontal transect within the drainage ~0.8–1.4 km northwest of our sample transect (Figures 3 and 6). Their zircon and top two apatite samples yield the same age, within 2 sigma error, to our zircon and apatite ages (Figure 7); the mean age for all these samples is 9.9 ± 2.3 Ma. Their three lowest elevation apatite samples yielded ages that decrease with elevation from 7.5 ± 1.6 Ma to 4.1 ± 1.1 Ma (mean age ±2 sigma error for the two lowest elevation samples), suggesting slow cooling through a Miocene-Pliocene apatite partial retention zone.

[15] At first glance, these two data sets appear to indicate a different exhumation history for the Kung Co granite despite their spatial proximity. Our data set is straightforward pointing to rapid exhumation at ~10 Ma, whereas M07's data set suggests a period of slow cooling during a longer time period. Furthermore, based on their data, M07 proposed initiation of normal faulting along this part of the Kung Co rift at ~4 Ma, significantly younger than what our data reveal. Because models proposed for the development of EW extension across the Tibetan Plateau make predictions about the timing of normal faulting, it is essential to determine an exhumation/cooling history consistent with both sets of data.

[16] To quantify the cooling and exhumation history of the footwall to the Kung Co fault, we completed inverse modeling of (U-Th)/He zircon and apatite ages (this study and M07) from the Kung Co granite, using the (U-Th)/He modeling software package (HeMP) [*Hager and Stockli*, 2009] (Figures 8, 9, 10, and 11). The advantage of HeMP over other software, for example HeFTy [*Ketcham*, 2005], is that it allows inverse modeling of multiple thermochronometer 1-D vertical sample transects. An overview of our approach including the basic equations solved within the HeMP software and other data are given in Appendix A. To model an entire transect, a randomly created thermal history is offset equally to higher temperatures using the vertical sample spacing and a range of user-defined geothermal gradients. Although randomly created, we chose to restrict the t-T space based on the following constraints. As a starting point, we

Notes to Table 1:

[a] All errors are 1σ. Sample KC57 (latitude/longitude is 28°46.537/86°28.957).

[b] Here r, rim; c, core; i, intermediate.

[c] Th/U ratios are based on measured ThO and U.

[d] Here f_{206} is the amount of ^{206}Pb contributed by common (i.e., non–in situ radiogenic) Pb based on ^{204}Pb. Figures in parentheses indicate that ^{204}Pb counts were indistinguishable from baseline and in these cases, no correction has been applied.

[e] Here n/a indicates that no common Pb correction has been applied.

[f] Here ^{207}Pb/^{206}Pb ages are reported only for older core analyses and intermediate rims where these are older than 100 Ma.

[g] Here 207-corrected ages are calculated by projecting from assumed common Pb (^{207}Pb/^{206}Pb = 0.83 ± 0.1) through the common Pb uncorrected data point onto concordia, implicitly assuming concordance. These are only reported when <1000 Ma. Ages in bold represent rim analyses included in our preferred age calculation.

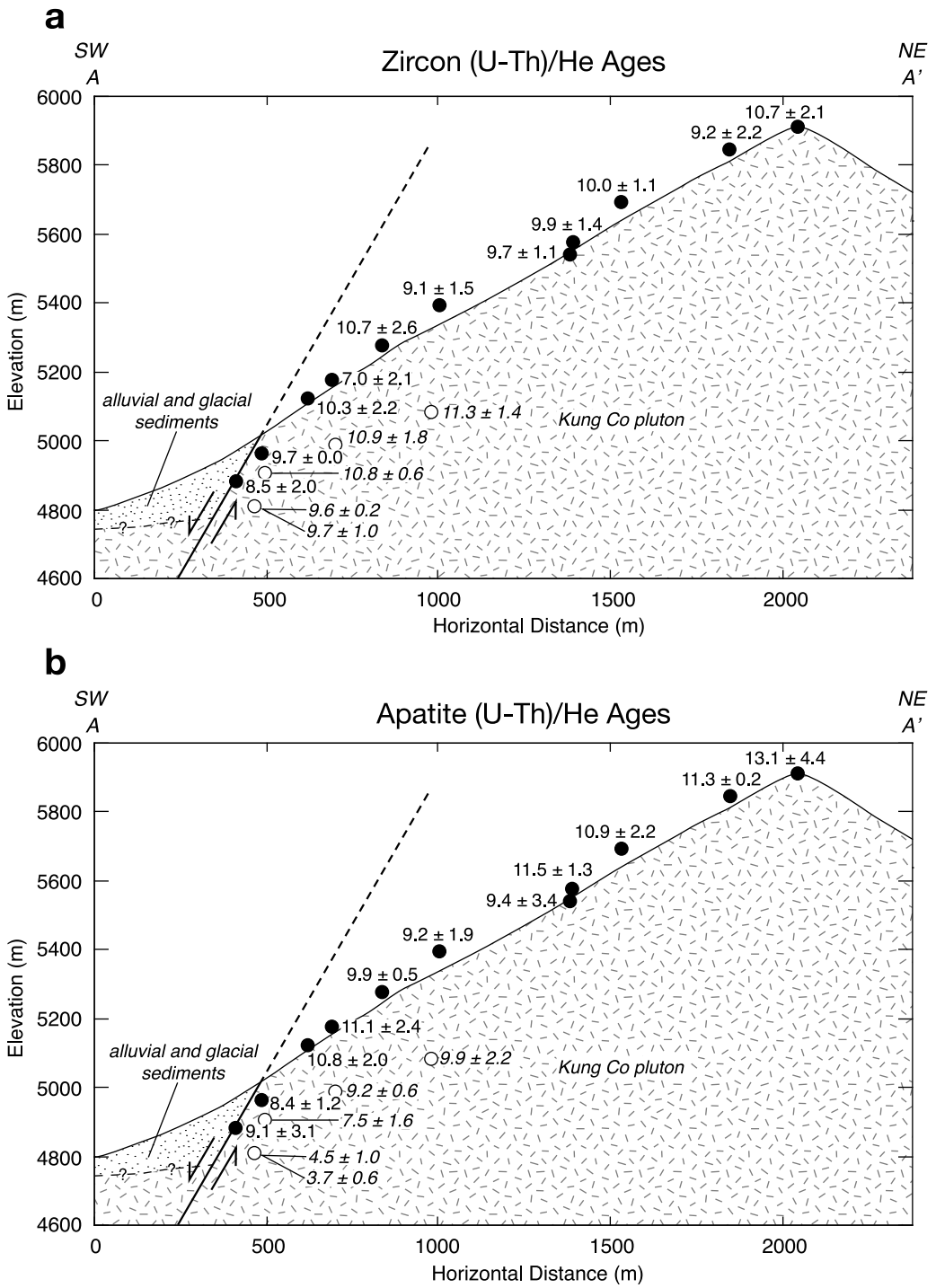

Figure 6. (a) Zircon and (b) apatite (U-Th)/He ages from this study (black circles and bold font) and M07 (white circles and italic font) projected onto an NE-SW cross section across the Kung Co granite. Location of cross section shown in Figure 3.

assigned a temperature range of 520°C–545°C at 18 Ma followed by mica $^{40}Ar/^{39}Ar$ age data reported by M07 (mean ±2 sigma biotite and muscovite age of 15.5 ± 1.7 Ma at 270°C–405°C). Given the overlap in zircon and apatite (U-Th)/He ages, a large box spanning the interval between 5°C and 220°C at 10.0 ± 2.0 Ma allows for rapid cooling below ~185°C and ~70°C, the estimated closure temperatures for zircon and apatite, respectively [*Wolf et al.*, 1996, 1998; *House et al.*, 1999; *Stockli et al.*, 2000; *Tagami et al.*, 2003; *Stockli*, 2005], to the estimated annual surface temperature of 5°C. The wide range of apatite ages in M07's data set could be the result of either very slow cooling through the apatite

Table 2. Zircon and Apatite (U-Th)/He Data

Sample	Latitude	Longitude	Elevation (m)	Mass (mg)	He (ncc/mg)	U (ppm)	Th (ppm)	F_t	Mean Age (Ma)	±2 Sigma (Ma)	Replicates[a]
This Study											
Zircon											
KC60	28°46.214	86°29.532	5945	7.1	701.2	681.6	56.9	0.77	10.7	2.2	3
KC59	28°46.319	86°29.322	5877	11.8	1747.3	1880.7	90.5	0.80	9.2	2.4	3
KC57	28°46.537	86°28.957	5700	15.3	1386.7	1361.8	119.3	0.82	10.0	1.1	3
KC56	28°46.110	86°29.121	5585	10.8	1580.2	1594.7	150.6	0.80	9.9	1.5	3
KC55	28°46.563	86°28.834	5500	8.1	1580.2	1639.7	129.3	0.77	9.7	1.0	3
KC54	28°46.180	86°28.795	5402	16.3	872.5	948.4	79.4	0.82	9.1	1.6	3
KC53	28°46.119	86°28.712	5279	7.8	1686.0	1563.1	138.4	0.77	10.7	2.6	3
KC52	28°46.010	86°28.677	5185	13.0	1310.3	1912.9	120.8	0.80	7.0	2.1	2
KC51	28°46.135	86°28.547′	5106	6.6	1871.6	1927.1	60.4	0.75	10.3	2.3	3
KC50	28°46.242	86°28.317	4981	5.8	611.2	683.6	60.9	0.73	9.8	0.6	3
KC49	28°46.258	86°28.244	4880	5.9	1070.5	1343.8	108.4	0.74	8.5	1.9	3
Apatite											
KC60	28°46.214	86°29.532	5945	7.0	68.1	52.4	3.8	0.82	13.2	4.1	6
KC59	28°46.319	86°29.322	5877	5.4	19.7	21.0	5.2	0.67	11.2	0.1	3
KC57	28°46.537	86°28.957	5700	3.5	11.4	8.8	10.2	0.68	11.0	2.4	3
KC56	28°46.110	86°29.121	5585	4.4	13.9	12.4	5.1	0.68	11.4	3.3	5
KC55	28°46.563	86°28.834	5500	3.7	12.7	13.3	5.5	0.70	9.3	3.5	3
KC54	28°46.180	86°28.795	5402	18.2	58.2	55.1	5.4	0.82	9.2	2.0	8
KC53	28°46.119	86°28.712	5279	4.5	80.2	96.8	3.3	0.68	9.8	0.7	4
KC52	28°46.010	86°28.677	5185	4.5	34.4	36.1	3.3	0.70	11.1	2.4	3
KC51	28°46.135	86°28.547′	5106	8.1	89.1	88.8	37.7	0.72	10.6	2.3	4
KC50	28°46.242	86°28.317	4981	9.6	63.2	67.9	4.9	0.90	8.2	1.3	5
KC49	28°46.258	86°28.244	4880	5.5	59.9	73.0	2.2	0.75	9.1	3.4	5
Mahéo Zircon and Apatite (U-Th)/He Data											
Zircon											
K2L175	28°46.780	86°28.398	5082	64.8	55.2	1055.3	89.5	0.82	11.3	1.4	4
K2L176	28°46.737	86°28.233	4987	61.1	50.1	950.7	129.6	0.85	10.9	1.8	3
K2P86	28°46.683	86°28.120	4904	42.2	49.8	1051.5	89.2	0.80	10.8	0.6	6
K2L172	28°46.662	86°28.000	4808	14.1	69.1	1807.5	113.5	0.74	9.6	0.2	2
K2L173	28°46.662	86°28.000	4808	44.0	33.5	767.5	82.5	0.80	9.7	1.0	2
Apatite											
K2L175	28°46.780	86°28.398	5082	9.6	1.9	41.2	34.1	0.76	9.9	2.2	3
K2L176	28°46.737	86°28.233	4987	14.3	1.7	40.0	3.6	0.82	9.2	0.6	2
K2P86	28°46.683	86°28.120	4904	10.1	2.1	57.4	55.4	0.74	7.5	1.6	3
K2L172	28°46.662	86°28.000	4808	7.2	0.5	28.8	29.6	0.74	3.7	0.6	4
K2L173	28°46.662	86°28.000	4808	5.6	1.4	52.7	131.5	0.73	4.5	1.0	3

[a]Number of replicates per sample. For this study, see Table S1 for replicate analyses; for the Mahéo data set, see *Mahéo et al.* [2007] for replicate analyses.

partial retention zone or a post exhumation reheating event. To incorporate both scenarios into our modeling, another constraint was added between 7 and 3 Ma to allow for an increase in temperature. Utilizing the algorithms described by *Ketcham* [2005], HeMP calculates model ages for each thermal history and evaluates the results against the corresponding sample ages based on a "goodness of fit" (GOF) criterion [*Ketcham et al.*, 2000]. The results are a family of random thermal histories consistent with the thermochronometric data and constraints on geothermal gradients. To fit thermal histories to our data set, we decreased the number of samples evaluated against the model ages to five and allowed three outliers. Model run parameters as well as number of acceptable solutions for each geothermal gradient are given in Figure 11. One of the challenges in the inverse modeling approach is providing enough guidance for the random t-T history generation to yield a meaningful number of solutions without missing possible cooling scenarios by over constraining the model. For both data sets, the acceptable cooling paths are well within our constraint boxes for the zircon and apatite data, evidence in support of the validity of our model setup.

6. Interpretation of Thermochronometric Data

[17] Results of inverse modeling of (U-Th)/He zircon and apatite ages (this study and M07) using HeMP are shown in Figures 9, 10, and 11. Our early modeling efforts showed that treating our and M07's data sets as one vertical transect did not yield any acceptable solutions and therefore had to be modeled independently for reasons explained later in this section. As a consequence, model results yield acceptable fits for zircon and apatite samples from this study and from M07, but at different geothermal gradients (Figures 9, 10, and 11). For samples from this study, geothermal gradients of 15°C–50°C/km yield acceptable thermal histories; the 15°C/km geothermal gradient yields the maximum number of acceptable thermal histories (Figures 9 and 11). However, the combination of an estimated pressure of <3 kbar (<8.1 km)

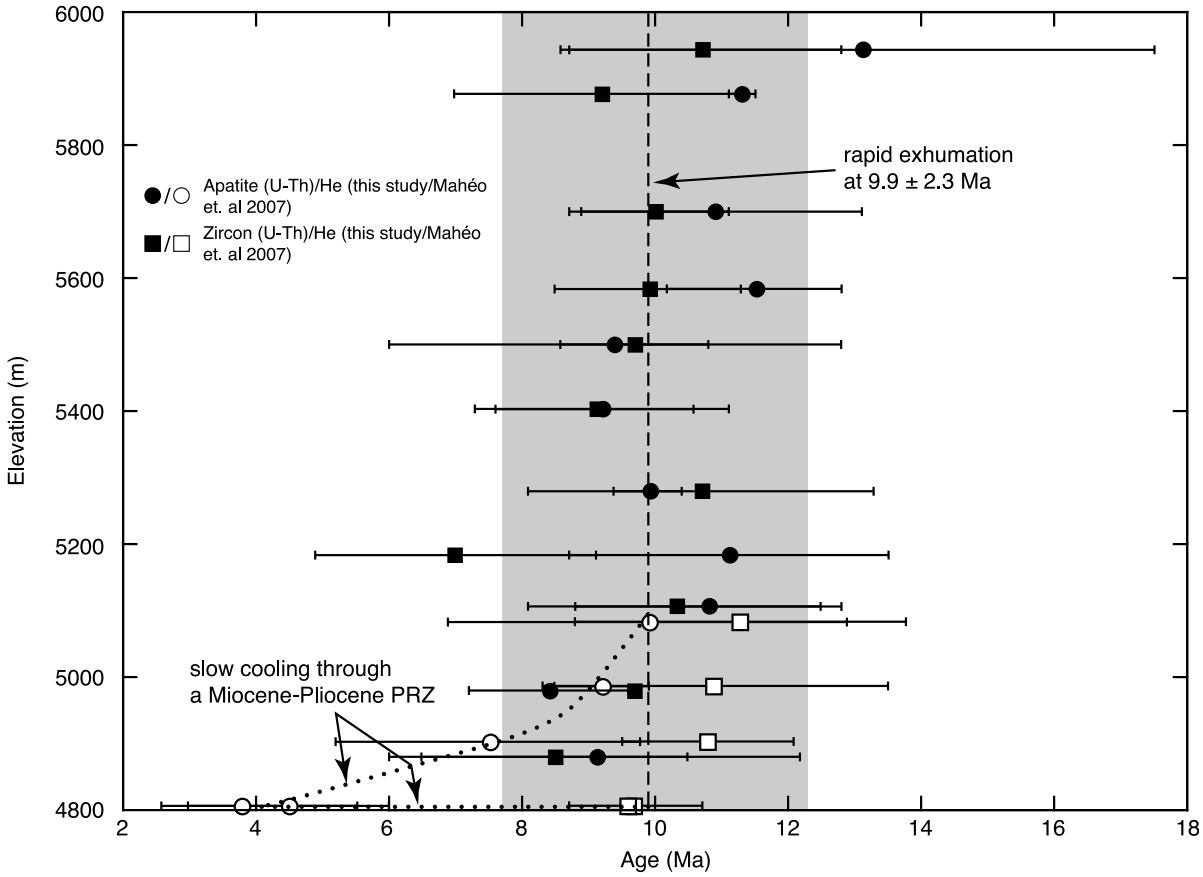

Figure 7. Plot of zircon and apatite (U-Th)/He ages from this study and M07 versus elevation showing the cooling history for the Kung Co footwall. Horizontal lines show 2σ error associated with each zircon and apatite sample. Dashed vertical line shows mean age of 9.9 Ma, and gray shaded column shows the associated 2σ error of 2.3 Ma for all zircons and all but the youngest apatite samples from this study and M07. Dotted lines bound the range of slow cooling histories through a Miocene-Pliocene partial retention zone.

in the contact metamorphic aureole of the Kung Co granite (M07) with postulated onset of exhumation at 12–13 Ma at temperatures of ~300°C (see discussion on synoptic cooling history below; Figure 12) suggest that a geothermal gradient of ~35°C/km is more reasonable. Inverse modeling results indicate that the Kung Co granite underwent rapid cooling from temperatures of ~420°C–275°C at ~15.5 Ma to temperatures of ~220°C at ~12–10 Ma (Figure 9). This rapid cooling event was followed by extreme rapid cooling (~280°C/Ma) from temperatures of ~200°C to ~60°C–5°C between ~12–10 Ma and ~9 Ma. Assuming a constant geothermal gradient of 15°C–50°C/km, this cooling rate implies that the 1065 m vertical section of the Kung Co granite was exhumed at a high rate of 19–6 mm/yr. This extreme rapid cooling episode was, in turn, followed by either slow cooling or quiescence from ~50°C–5°C to a surface temperature of ~5°C since ~9 Ma or slow cooling to a surface temperature of ~5°C interrupted by a minor reheating event characterized by a ≤40°C increase in temperature between ~8 and 4 Ma (Figure 9).

[18] Model results for zircon and apatite samples from M07 yield acceptable fits for geothermal gradients of 110°C–300°C/km (Figures 10 and 11), considerably higher than for samples from this study. A geothermal gradient of 180°C/km yields the maximum number of acceptable thermal histories and indicates that the Kung Co granite underwent rapid cooling from temperatures of ~400°C–270°C at ~15.5 Ma to temperatures of ~220°C–180°C at 10–12 Ma (Figures 10 and 11). This rapid cooling event was followed by very rapid cooling (~100°C/Ma) as temperatures dropped from ~150°C to ~30°C–5°C between ~10 Ma and ~9 Ma. Cooling of the footwall ended with either slow cooling from ~30°C–10°C to a surface temperature of ~5°C or slow cooling to a surface temperature of ~5°C interrupted by a minor reheating event characterized by a ≤25°C increase in temperature between ~7 and 5 Ma (Figure 10).

[19] We suggest that the similar model cooling histories for samples from this study and from M07, but under different geothermal gradients, is a consequence of sample location with respect to the range-bounding fault (Figure 6). The zircon and apatite samples from our study were collected along the exhumed footwall escarpment over a vertical distance of ~1065 m (Figures 2, 3, and 6). In contrast, M07's samples were collected from a river valley and therefore deeper (a horizontal distance of between ~105 and 780 m) from within the Kung Co granite relative to the range-

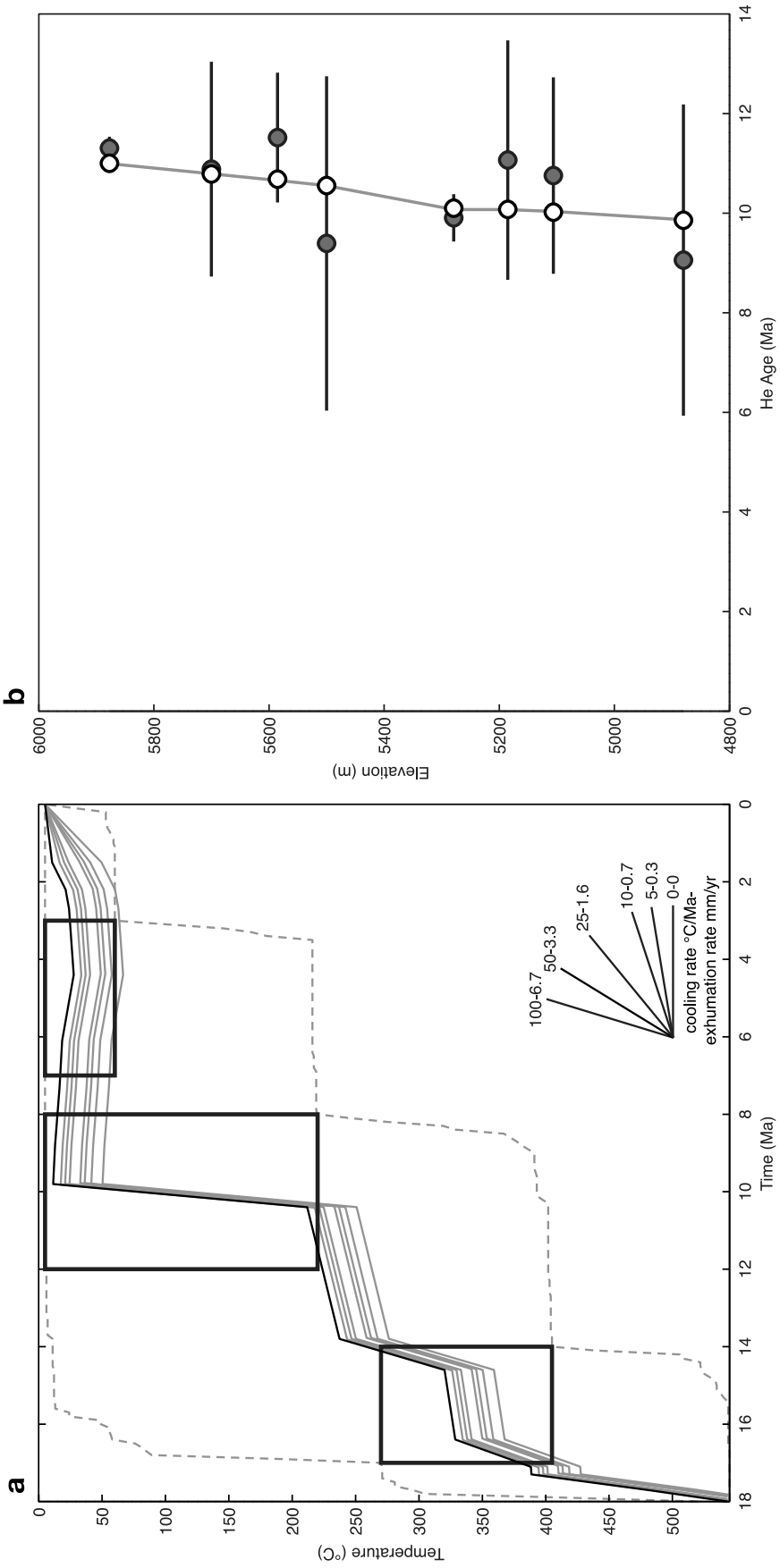

Figure 8. Graphical representation of our model approach for generating a cooling history from apatite (U-Th)/He ages collected from our vertical transect. (a) Time-temperature (t-T) path in black represents the initial, randomly created thermal history for the topmost sample. Offset t-T paths in gray are generated using sample spacing and a user-defined geothermal gradient simulating temperature conditions for each sample at depth. Black boxes are time-temperature bounds for mica $^{40}Ar/^{39}Ar$, zircon (U-Th)/He, and apatite (U-Th)/He. Dashed gray lines bound the t-T space covered by 100,000 randomly created model thermal histories. Exhumation rates shown on the cooling rate–exhumation rate reference curves are based on a 15°C/km geothermal gradient. (b) Age versus elevation plot showing apatite sample ages (dark gray circles) and model ages derived from this set of t-T histories (white circles). Gray line connecting the model ages is equivalent to the graphical result shown in Figure 9.

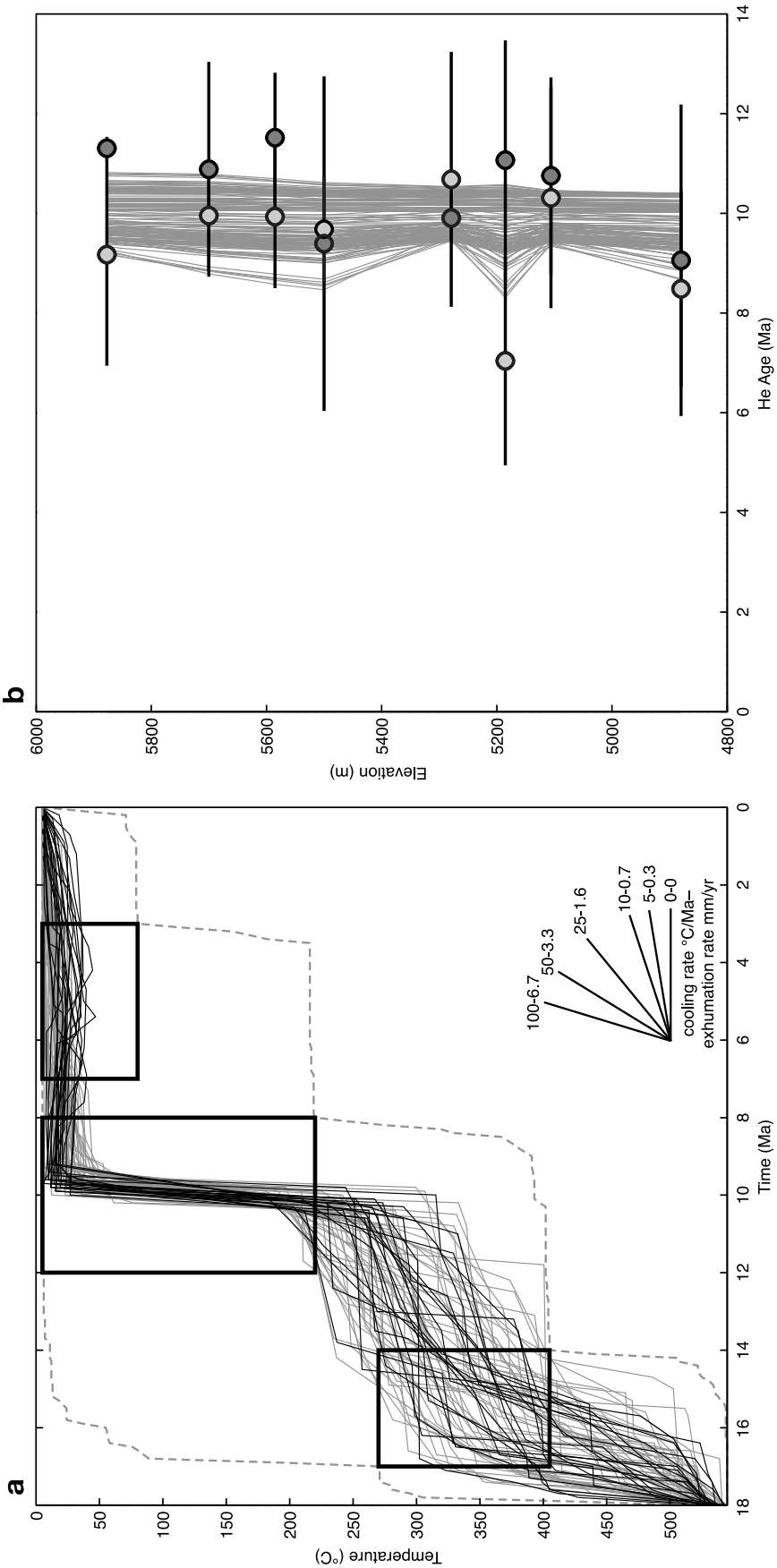

Figure 9. Model HeMP cooling histories for zircon and apatite (U-Th)/He samples collected in this study using a 15°C/km geothermal gradient, the geothermal gradient that yields the largest number of acceptable cooling histories (Figure 11a). (a) Model cooling curves plotted on a time-temperature graph. Solid gray curves do not yield a reheating event, whereas black curves yield a minor reheating event between ~8 and 4 Ma. Black boxes are time-temperature bounds for mica $^{40}Ar/^{39}Ar$, zircon (U-Th)/He, and apatite (U-Th)/He. Dashed gray lines bound the t-T space covered by 100,000 randomly created model thermal histories. Exhumation rates shown on the cooling rate–exhumation rate reference curves are based on a 15°C/km geothermal gradient. (b) Model cooling histories plotted on a (U-Th)/He age-elevation graph. Light gray circles are zircon, and dark gray ones are apatite. Error bars are two-sigma.

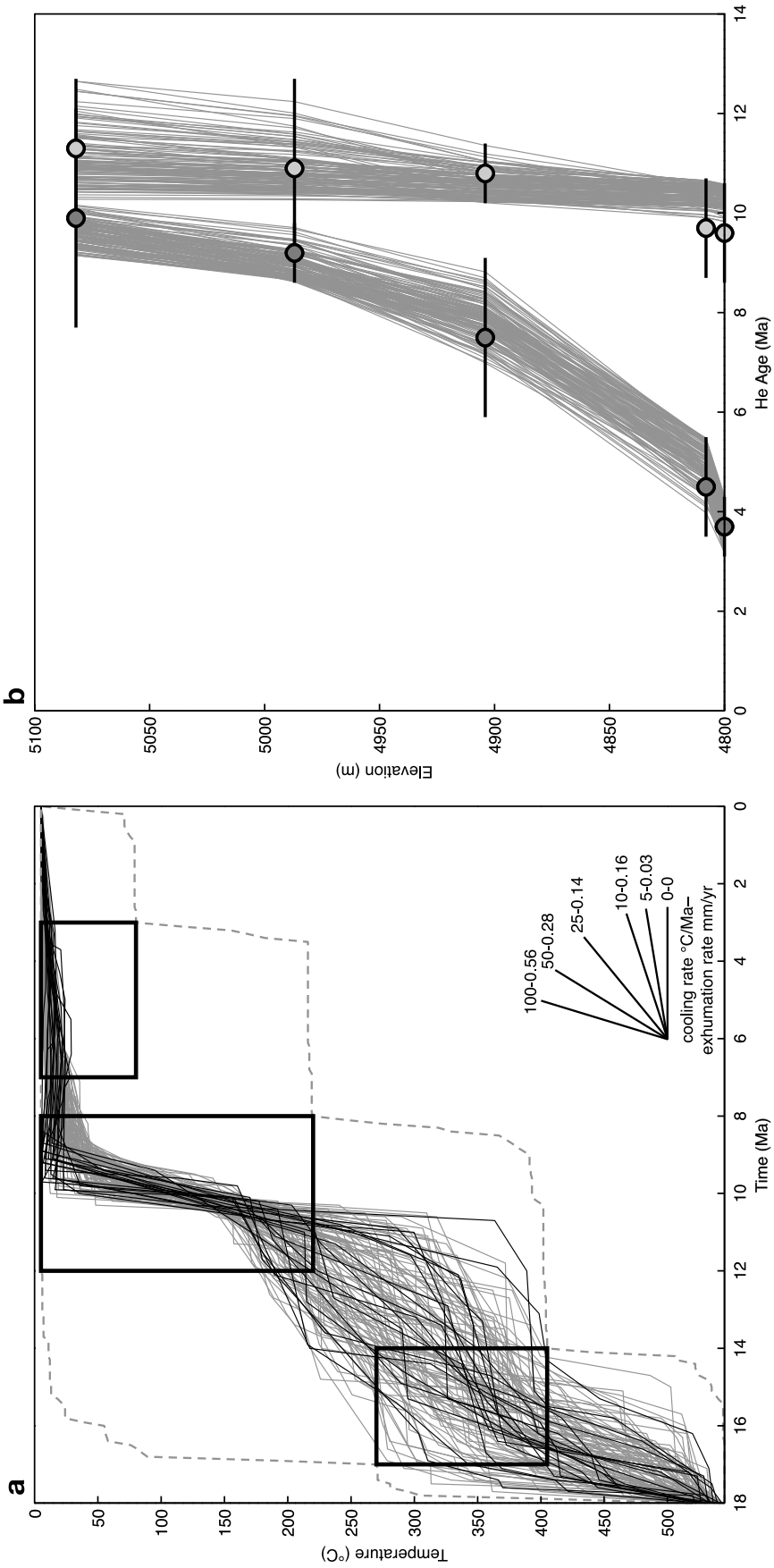

Figure 10. Model HeMP cooling histories for zircon and apatite (U-Th)/He samples collected by M07 using a 180°C/km geothermal gradient, the geothermal gradient that yields the largest number of acceptable cooling histories (Figure 11b). (a) Model cooling curves plotted on a time-temperature graph. Solid gray curves did not yield a reheating event, whereas black curves yield a minor reheating event between ~7 and 5 Ma. Black boxes are time-temperature bounds for mica $^{40}Ar/^{39}Ar$, zircon (U-Th)/He, and apatite (U-Th)/He. Dashed gray lines bound the t-T space covered by 100,000 randomly created model thermal histories. The exhumation rates shown on the cooling rate–exhumation rate reference curves are based on a 180°C/km geothermal gradient. (b) Model cooling histories plotted on a (U-Th)/He age-elevation graph. Light gray circles are zircon, and dark gray ones are apatite. Error bars are two-sigma.

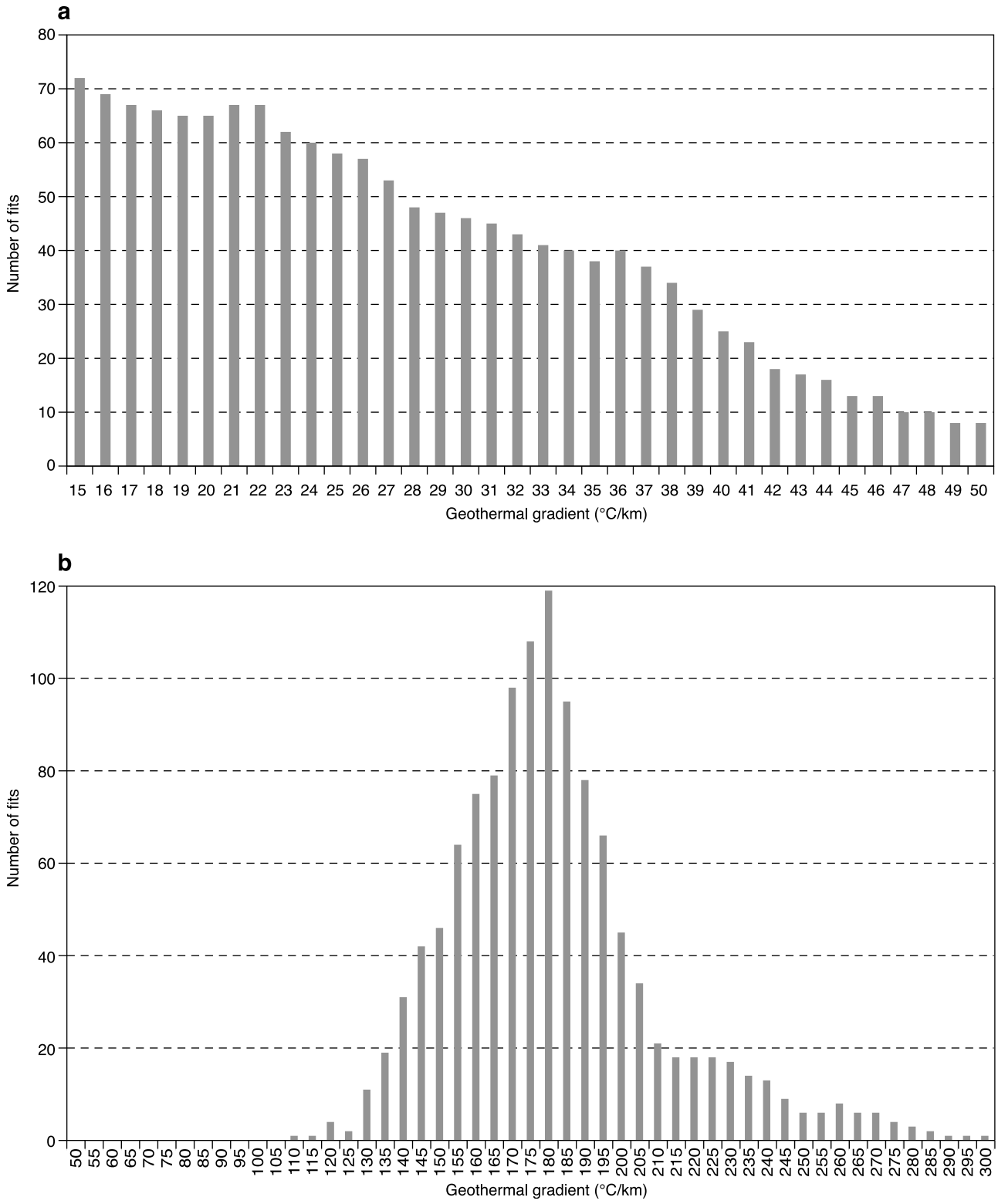

Figure 11. Histograms showing the number of HeMP model generated cooling histories that successfully fit zircon and apatite (U-Th)/He age data (a) from this study and (b) from M07 for a given geothermal gradient.

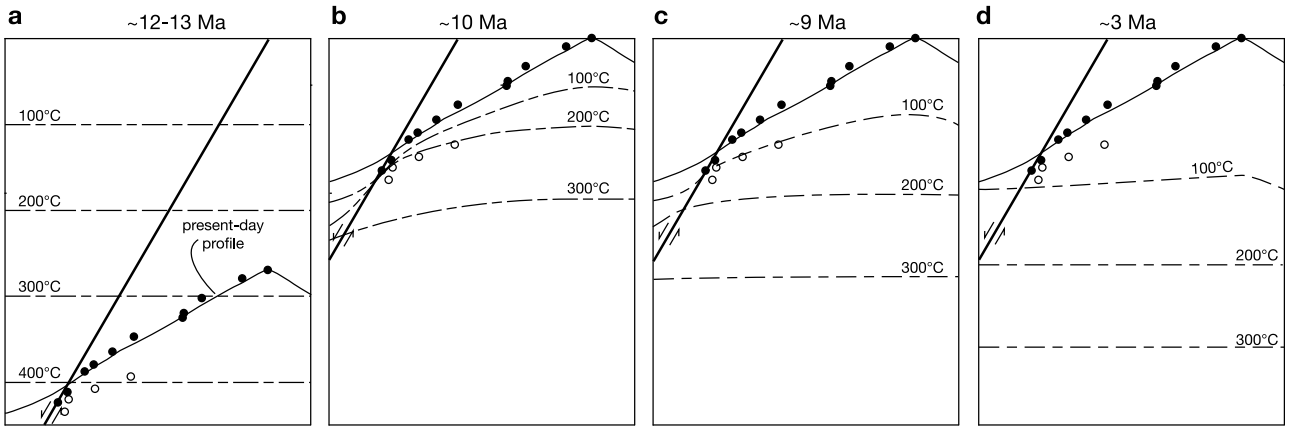

Figure 12. Schematic evolutionary cross sections showing location of (U-Th)/He zircon and apatite samples from this study (solid circles) and M07 (open circles) with respect to isotherms at different time intervals. (a) Prior to 10 Ma, samples were below ~185°C, the estimated closure temperature for zircons. The modeled geothermal gradient is ~15°C/km, although it could have been as high as 50°C/km. (b) Extreme rapid exhumation at ~10 Ma resulted in samples from this study cooling below both the zircon and apatite closure temperatures (~185°C and 70°C, respectively). Advection of mass and heat results in convex up and compressed isotherms in footwall. Because M07's samples are located distal with respect to the Kung Co fault, they were still above 185°C. (c) M07's samples cooled through closure isotherms at slightly different times as the footwall thermally reequilibrated. The zircon samples cooled rapidly as isotherms initially reequilibrated rapidly. Relatively high elevation apatite samples also initially cooled relatively rapidly. (d) As the thermal reequilibration rate decayed with time, the deepest apatite samples underwent progressively slower cooling between ~9 and ~4.1 Ma. Present-day profile is from the cross section shown in Figure 6. See text for discussion.

bounding fault (Figures 3 and 6). Two-dimensional numerical studies show that normal faulting, accompanied by footwall erosion and hanging wall sedimentation, result in upward advection of isotherms in the footwall and downward advection of isotherms in the hanging wall. The consequence is compressed convex up footwall and concave up hanging wall isotherms that can mimic topography [*Ehlers and Chapman*, 1999; *Ehlers et al.*, 2001; *Ehlers and Farley*, 2003]. As a result, (U-Th)/He samples collected in close proximity to the fault will record a cooling history that is different to those samples collected distal to the fault and, therefore, from deeper within the footwall (Figure 12).

[20] We postulate that extreme rapid exhumation (19–6 mm/yr) in the footwall of the Kung Co normal fault locked in zircon and apatite samples from this study at the same apparent (U-Th)/He age of ~10 Ma (Figures 7, 9b, and 12). Given a 60° dipping fault, this exhumation rate implies a fault slip rate of 21.9–6.9 mm/yr. Advection of the footwall resulted in convex-up isotherms that mimicked the geometry of the range front fault (Figure 12b). The result was compression of isotherms and a short-lived elevated geothermal gradient of between 100°C and 300°C/km soon after which samples from this study cooled below ~185°C and ~70°C, the estimated closure temperatures for zircon and apatite. In contrast, M07's samples, collected over a horizontal distance rather than a vertical one, were located deeper into the footwall and distal to the range front fault relative to our samples. Therefore, because of the compressed, advected isotherms, M07's samples were still above 185°C (Figure 12b). During thermal reequilibration following extreme rapid exhumation, all of M07's samples cooled relatively quickly through the zircon closure temperature causing a near vertical age versus elevation trend (Figures 7, 10b, 12b, and 12c). The topmost of M07's samples also initially cooled relatively rapidly through the apatite closure temperature, however as the thermal reequilibration rate decayed with time, the deepest samples underwent progressively slower cooling between ~9 and 4.1 Ma (Figures 7, 9b, 12c, and 12d).

[21] A few of the model cooling curves yield a transient and small (≤40°C) reheating event between ~8 and 4 Ma for the lowest elevation samples at the range front (Figures 9a and 10a). If reheating did occur, hydrothermal activity along the fault is a plausible explanation. Although springs are exposed along the Butra Ree segment of the fault, M07 and we did not observe evidence for hydrothermal activity.

[22] A reasonable synoptic cooling history and interpreted fault slip history for the Butra Ree segment of the Kung Co rift, based on our zircon U/Pb, M07's mica $^{40}Ar/^{39}Ar$, and our and M07's zircon and apatite (U-Th)/He age data, is shown in Figure 13. To characterize cooling of the Kung Co granite following emplacement at depths of ~8 km (<3 kbar), we completed two-dimensional thermal modeling using Heat3D (K. Wohletz, Kware HEAT3D (v4.11.0533) software, 2008; available at http://geodynamics.lanl.gov/Wohletz/Heat.htm#Download) (Table 3). Model results show that the Kung Co granite initially exhibited very rapid cooling at rates of ~600°C–40°C/Ma due to thermal reequilibration following emplacement at 19.1 ± 0.5 Ma at a zircon U/Pb closure temperature of ~720°C [*H. Zhang et al.*, 2004]. During the waning stages of thermal reequilibration, cooling rates

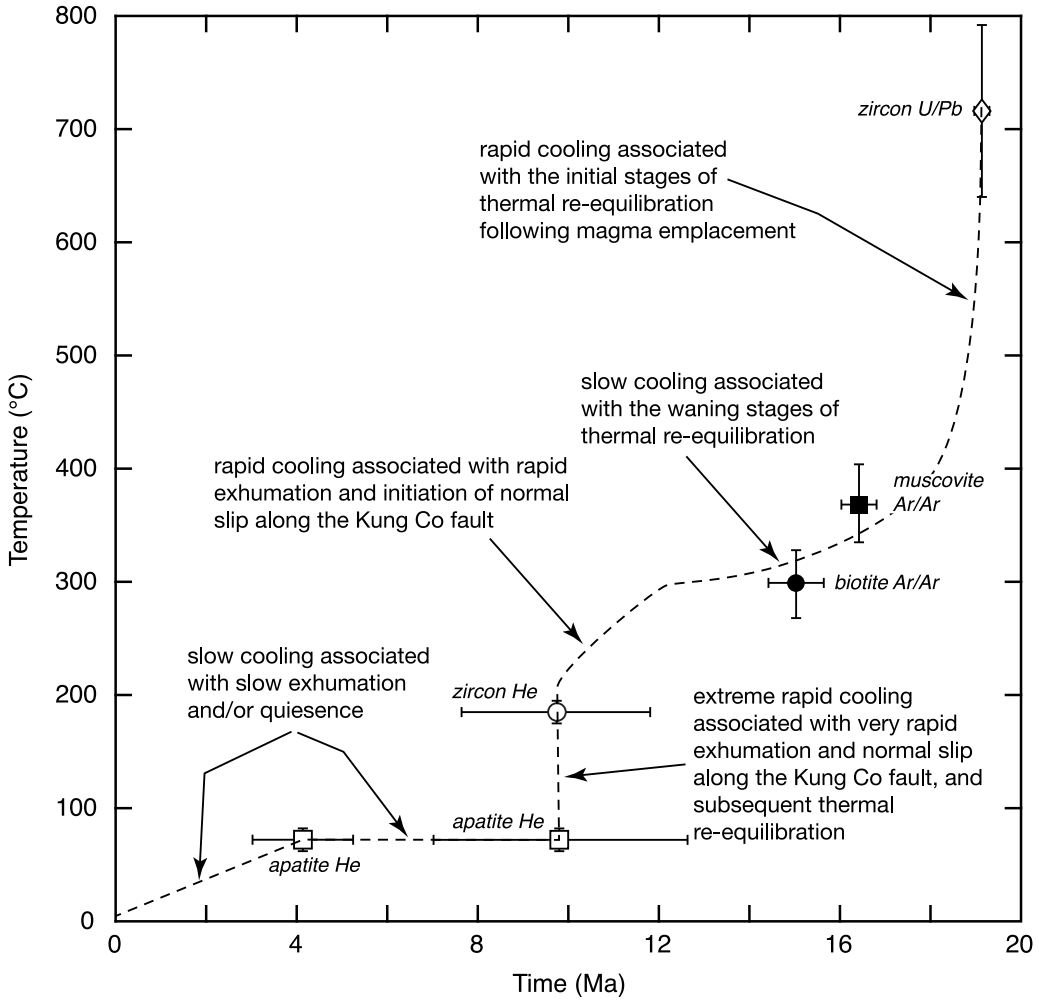

Figure 13. Time-temperature plot showing a reasonable cooling history for the Kung Co granite and interpreted fault slip history along the Butra Ree segment of the Kung Co normal fault. See text for discussion.

dramatically decreased to ~3°C–1°C/Ma as temperatures dropped toward ~300°C and micas closed to argon loss at ~15.5 Ma. Post emplacement thermal reequilibration was followed by rapid cooling, at rates of ~40°C/Ma, associated with a rapid exhumation and initiation of slip along the Kung Co fault between ~12.5 and 10.0 Ma. Extreme rapid exhumation, cooling at rates of ~280°C/Ma, of the Kung Co granite indicate an acceleration in slip rate (fault slip rate of 21.9–6.9 mm/yr) along the Kung Co normal fault at ~10.0 Ma. This episode of extreme rapid cooling was followed by thermal reequilibration at ~10–9 Ma as temperatures throughout most of the exhumed footwall dropped from ~200°C to <70°C. Postfaulting thermal reequilibration was, in turn, followed by slow cooling at rates of ≤5°C/Ma associated with either slow exhumation and minor fault slip and/or quiescence between ~9 Ma and present day.

7. Timing of Extension Across the Tibetan Plateau

[23] In general, the initiation of approximately EW extension across the Tibetan Plateau is middle to late Miocene, although the data set is small (Figure 14). All but one study has been completed in southern Tibet, south of the Banggong

Table 3. HEAT3D Model Variables[a]

	Bedrock					Magma			
Model Number	Surface T°C	Geothermal Gradient (°C/km)	Thermal Conductivity ($W\ m^{-1}\ K^{-1}$)	Specific Heat Capacity (J/kg K)	Density (kg/m^3)	Dimensions (Width km × Thickness km)	Thermal Conductivity ($Wm^{-1}\ K^{-1}$)	Specific Heat Capacity (J/kg K)	Melting Temperature (°C)
15	5	30	2.0	970	2700	26 × 10	2.0	1260	720

[a]Grid size, 1.0 km; bedrock dimensions (width × thickness), 50 km × 70 km; magma top, 8 km. Specific heat capacities calculated using the work of *Whittington et al.* [2009].

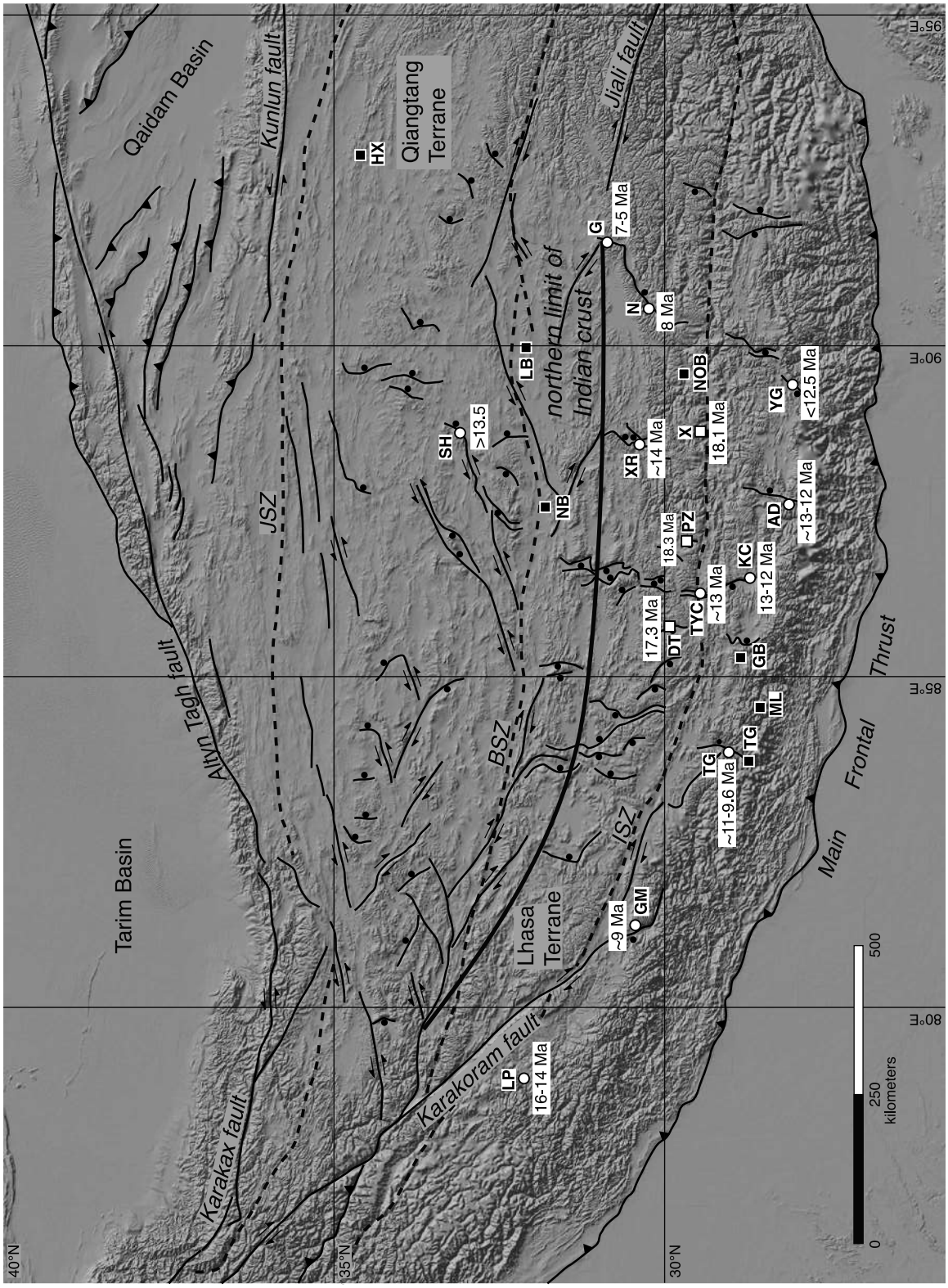
Qaidam Basin
Kunlun fault
Altyn Tagh fault
Karakax fault
Karakoram fault
JSZ
BSZ
ISZ
Tarim Basin
Lhasa Terrane
Qiangtang Terrane
northern limit of Indian crust
Jiali fault
Main Frontal Thrust
HX
LB
NB
SH
>13.5
XR
~14 Ma
X
NOB
18.1 Ma
YG
<12.5 Ma
AD
~13-12 Ma
KC
13-12 Ma
PZ
18.3 Ma
TYC
~13 Ma
DT
17.3 Ma
GB
TG
~11-9.6 Ma
ML
TG
GM
~9 Ma
LP
16-14 Ma
N
8 Ma
G
7-5 Ma
40°N
35°N
30°N
80°E
85°E
90°E
95°E
0
250
500
kilometers

Figure 14

suture zone. Our study in the Kung Co rift suggests initiation of extension at ~12–13 Ma with an accelerated episode at ~10 Ma. Zircon and apatite (U-Th)/He thermochronometry across the footwall of the Tangra Yum Co rift, the northern continuation of the Kung Co rift, indicates two episodes of exhumation, the oldest at ~13 Ma and a younger, more dominant one at ~6 Ma [*Dewane et al.*, 2006]. To the southeast in the Ama Drime massif, exhumation and associated decompression melting at 13–12 Ma are interpreted as the result of orogen-parallel extension [*Cottle et al.*, 2009; *Kali et al.*, 2010]. Farther to the east, EW extension across the Yadong rift, which cuts the STDS, must be <12.5 Ma because the STDS cuts the ~12.5 Ma Kula Kangri granite [*Edwards and Harrison*, 1997]. To the west of Kung Co, minor normal faulting begin at ~11–9.6 Ma during deposition of the Tetang Formation in the NS trending Thakkhola graben [*Garzione et al.*, 2003]. In Marsyandi valley, southeast of the Thakkhola graben, muscovite from a hydrothermal vein within a NS trending fracture yielded an ~14 Ma $^{40}Ar/^{39}Ar$ age, inferred as the onset of extension here [*Coleman and Hodges*, 1995]. However, M07 suggest an alternative interpretation whereby these fractures developed in response to NS contraction, a consequence of a horizontal NS oriented maximum stress, σ_1, and vertical intermediate principle stress, σ_2. $^{40}Ar/^{39}Ar$ on micas collected from the footwall of the Gurla Mandhata detachment fault and magnetostratigraphy in its superdetachment basin, the Zhada basin, suggests that orogen parallel extension here started at ~9 Ma [*Murphy et al.*, 2002; *Saylor et al.*, 2009, 2010] and possibly as early as ~15 Ma [*Murphy and Copeland*, 2005]. Note that the Gurla Mandhata area defines a local pull-apart structure along the Karakorum strike-slip fault, and therefore, may not be associated with regional extension. Farther to the west, $^{40}Ar/^{39}Ar$ on micas in the footwall of the Leo Pargil detachment [*Thiede et al.*, 2006] and on synkinematic muscovites on NS striking normal faults within the footwall of the Leo Pargil detachment [*Hintersberger et al.*, 2010] suggest onset of EW extension here at 17–14 Ma, the oldest age for initiation of normal faulting in southern Tibet. *Hintersberger et al.* [2010] attributed extensional deformation to the west of the Karakorum fault because that fault did not accommodate the EW extensional strain on the Tibetan Plateau.

[24] A few studies on the timing of EW extension along normal faults have been completed within the Lhasa terrane to the north of the Indus-Tsangpo suture zone (Figure 14). Toward the eastern side of the Lhasa terrane, $^{40}Ar/^{39}Ar$ data on potassium feldspar from the Nyainqentanghla massif in the footwall of the Yangbajian graben suggests extension here initiated at ~8 Ma [*Harrison et al.*, 1995]. In the northeastern part of this rift system, the Gulu rift, apatite (U-Th)/He thermochronometry across footwall rocks implies that extension started 7–5 Ma [*Stockli et al.*, 2002]. In the central part of the Lhasa terrane, zircon and apatite (U-Th)/He thermochronometry across the footwall of the Xainza rift suggests that extension initiated at ~14 Ma along the northern portion of the rift with an accelerated episode of extension at 10–6 Ma along the length of the rift [*Hager et al.*, 2009]. In contrast to the timing of normal faulting, a number of ~18–17 Ma NS trending dikes exposed just north of the Indus-Tsangpo suture zone suggest an episode of early Miocene extension [*Williams et al.*, 2001] (Figure 14). These dikes may indicate an early, minor episode of EW extension [*Kapp and Guynn*, 2004] or they were emplaced in a stress field characterized by horizontal NS σ_1 and vertical σ_2 (i.e., NS contraction) [*Molnar*, 2005; M07].

[25] Finally, the only estimate for onset of extension from north of the Banggong suture zone in the Qiangtang block is in the Shuang Hu rift, where $^{40}Ar/^{39}Ar$ and Rb/Sr geochronologic results on mineralization within the main bounding normal fault are interpreted to indicate that extension began before 13.5 Ma [*Blisniuk et al.*, 2001] (Figure 14). However, as with the Gurla Mandhata area, the Shuang Hu rift defines a pull-apart structure associated with a step along a strike-slip fault and may not have developed in response to regional extension [*Molnar*, 2005]. Alternatively, *Taylor et al.* [2003] noted that the conjugate strike-slip faults that bound the Banggong suture zone (Figure 14) are kinematically linked to north striking normal faults to the south of the suture and NE striking normal faults to the north. Analysis of earthquake moment tensors across the plateau show that about half of the extension is accommodated by normal faulting and half by strike-slip faulting [*Molnar and Lyon-Caen*, 1989]. Thus, the two data sets indicate that the kinematically linked normal and strike-slip faults accommodate constrictional strain char-

Figure 14. Shaded relief map of the Tibetan Plateau showing major active faults. Ages are estimates of initiation for EW extension based on emplacement of NS striking dikes (white-filled squares) [*Yin et al.*, 1994; *Williams et al.*, 2001] and interpreted slip along normal faults (white filled circles) [*Harrison et al.*, 1995; *Edwards and Harrison*, 1997; *Blisniuk et al.*, 2001; *Williams et al.*, 2001; *Murphy et al.*, 2002; *Stockli et al.*, 2002; *Garzione et al.*, 2003; *Murphy and Copeland*, 2005; *Dewane et al.*, 2006; *Thiede et al.*, 2006; *Cottle et al.*, 2009; *Hager et al.*, 2009; *Saylor et al.*, 2009; *Hintersberger et al.*, 2010; *Kali et al.*, 2010] (also this study). Abbreviations for extension locations are as follows: AD, Ama Drime; DT, Daggyai Tso; G, Gulu; GM, Gurla Mandhata; KC, Kung Co; LP, Leo Pargil; N, Nyainqentanghla; PZ, Pabbai Zong; TG, Thakkhola graben; SH, Shuang Hu; TYC, Tangra Yum Co; X, Xigaze; XR, Xainza rift; YG, Yadong graben. Paleoaltimetry study locations (black filled squares) abbreviations are as follows: GB, Gyirong basin; HX, Hoh Xi basin; LB, Lunpola basin; ML, Manaslu leucogranite; NB, Nima basin; NOB, Namling-Oiyug basin; TG, Thakkhola graben. Solid teeth on the hanging wall of thrust faults, solid ball on the hanging wall of normal faults, and arrow pairs indicate sense of relative motion across strike-slip faults. Suture zone abbreviations are as follows: BSZ, Banggong suture zone; ISZ, Indus-Tsangpo suture zone; JSZ, Jinsha suture zone. Heavy black line shows surface projection of inferred northern limit of underthrust Indian crust from *Nabelek et al.* [2009]. Map modified from *Taylor et al.* [2003] and *Kapp and Guynn* [2004].

acterized by concurrent EW extension and NS contraction [e.g., *Taylor et al.*, 2003; *Mercier et al.*, 1987]. Furthermore, the geometry of strain accumulation based on GPS data, wherein eastward extension is approximately twice the northward convergence rate [*P.-Z. Zhang et al.*, 2004], is consistent with this geometry of strain release.

8. Models for Extension Across the Tibetan Plateau

[26] Given the caveat that the amount of data on the initiation age of extension across the Tibetan Plateau is limited, we can reach the following conclusions. NS striking dikes imply that minor EW extension initiated at ~18 Ma, although as described above this need not be the case. Onset of slip along approximately NS striking normal faults occurred at ~14–10 Ma, and was followed by major pulse of accelerated normal slip at ~10–6 Ma. This suggests that a state of stress with a vertical σ_1 and EW horizontal σ_3 was established in the early Miocene, but one or two major events subsequently occurred to cause onset of normal faulting and an acceleration of fault slip a few million years later.

[27] Although the timing of EW extension across the Tibetan Plateau is broadly similar, the lithospheric structure is not. Southern Tibet (south of ~31°N) is underlain by ~78 km thick crust and a relatively low density upper crust, and cold, high-density lower crust and lithospheric mantle interpreted to be Indian lower crust and mantle lithosphere [e.g., *Nelson et al.*, 1996; *Owens and Zandt*, 1997; *Rodgers and Schwartz*, 1997, 1998; *Kind et al.*, 2002; *DeCelles et al.*, 2002; *Shi et al.*, 2004; *Priestley et al.*, 2008; *Nabelek et al.*, 2009]. In contrast, northern Tibet (north of ~31°N) is underlain by somewhat thinner crust at ~65 km and hot, lower-density lower crust and lithospheric mantle, interpreted as southward descent of Eurasian lithosphere [e.g., *Owens and Zandt*, 1997; *Molnar et al.*, 1993; *Kosarev et al.*, 1999; *Rodgers and Schwartz*, 1998; *Kind et al.*, 2002]. The different lithospheric structures imply that the processes that drove the onset of extension across the Tibetan Plateau during the middle to late Miocene were either the same or, if different, were broadly simultaneous.

[28] Convective removal of lithospheric mantle and replacement by hot asthenospheric mantle [e.g., *England and Houseman*, 1989; *Jiménez-Munt and Platt*, 2006] was an early, and popular, hypothesis as an underlying cause for the increase in surface height of the plateau and resultant increase in gravitational potential energy that, in turn, were the driving forces for extension across the plateau. However, low S wave velocities in northern Tibet do not require that asthenosphere is present beneath the Moho [*Rodgers and Schwartz*, 1998], and SKS anisotropy observations [e.g., *Huang et al.*, 2000] and surface wave modeling [*Priestley et al.*, 2006, 2008] suggest that lithospheric mantle is present between lower Indian crust and asthenosphere beneath southern Tibet.

[29] *Harrison et al.* [1992] and *Molnar et al.* [1993] argued that the onset of EW extension on the plateau was triggered when Tibet reached its maximum elevation, and thus maximum gravitational potential energy. If this is the case, then based on the timing of extension across the plateau, maximum elevation was reached at middle to late Miocene time. Several studies, including stable isotope studies of basin sediments and micas within the northern and central Tibetan Plateau and within the Himalaya [*France-Lanord et al.*, 1988; *Garzione et al.*, 2000a, 2000b; *Rowley et al.*, 2001; *Currie et al.*, 2005; *Cyr et al.*, 2005; *Rowley and Currie*, 2006; *DeCelles et al.*, 2007] and leaf morphology in central Tibet [*Spicer et al.*, 2003] have addressed paleoaltimetry and the timing of high elevations across the plateau (Figure 14). In northeastern Tibet, *Cyr et al.* [2005] used a combination of oxygen and carbon isotopes and Mg/Ca ratios from carbonates in the Hoh Xil basin to infer that this basin has undergone significant surface uplift (>2.7 km) since ~39 Ma. In central Tibet, stable isotopic data from carbonate sediments and paleosols in the Lunpola basin suggest that this part of the plateau was at an elevation of >4 km since 35 ± 5 Ma [*Rowley and Currie*, 2006]. Approximately 240 km to the west in Nima basin, stable isotopic and geochronologic studies of an ancient carbonate paleosol imply that central Tibet was at 4.5–5 km by 26 Ma [*DeCelles et al.*, 2007]. In the Namling-Oiyug basin, *Spicer et al.* [2003] used the empirical relationship between leaf morphology and atmospheric properties related to altitude to conclude that this basin was at elevations of ~4.6 km at 15 Ma. Stable isotopic data on pedogenic and diagenetic carbonates from the same basin were inferred to show that this part of the plateau achieved an elevation of ~5.2 km by 15 Ma [*Currie et al.*, 2005], the same within error of *Spicer et al.*'s [2003] estimate. In the Himalaya, *Rowley and Garzione* [2007] modeled depleted δ^2H in micas from Manaslu leucogranite and Chhokang Arm [*France-Lanord et al.*, 1988] to postulate that this region has been at ~6100 m since the time of emplacement of Manaslu plutonic complex at ~20 Ma [*Harrison et al.*, 1999]. A combination of stable isotopic and geochronologic data from the Thakkhola and Gyirong basins suggest they were at elevations of 4.5–6.3 km and ~5.8 km by 11 Ma and 7 Ma, respectively [*Garzione et al.*, 2000a, 2000b; *Rowley et al.*, 2001]. In summary, paleoaltimetry data from the Lunpola, Nima, and Namling-Oiyug basins, and the Himalayas imply little if any change in elevation across much of the plateau since ~35 Ma, 26 Ma, 15 Ma, and 20 Ma, respectively.

[30] If these limited paleoaltimetry data are representative of Tibet's mean elevation, then the onset of normal faulting across the plateau during the middle to late Miocene and accelerated pulse of extension during the late Miocene are not correlated with increase in plateau elevation. An outcome of this conclusion is that the postulated convective removal of mantle lithosphere at ~8 Ma [*Molnar et al.*, 1993] is an unlikely explanation for rapid increase in elevation and associated onset of EW extension [*Rowley and Garzione*, 2007].

[31] Other early models for EW extension across the plateau, including basal shear caused by oblique convergence [*McCaffrey and Nabelek*, 1998; *Liu and Yang*, 2003] and oroclinal bending [*Klootwijk et al.*, 1985], predict that extension should be restricted to southern Tibet. Furthermore, the three-dimensional viscoelastic model of *Liu and Yang* [2003] shows that basal shear hinders extension in central and northern Tibet. Both of these predictions are inconsistent with observations that NS striking grabens and kinematically

linked strike-slip faults are exposed as far north as the northern side of the Qiangtang terrane (Figure 14).

[32] *DeCelles et al.* [2002] proposed a model whereby the upper crust of Tibet underwent EW extension to accommodate the slab of underthrust Indian lower crust that tapered northward vertically and horizontally beneath southern Tibet. This model predicts greater extension in the south (south of the Banggong suture zone) and a northward decrease in onset age of extension. The former is consistent with the geomorphic expression of normal faulting, which is much more pronounced in the south compared to the north [*Fielding et al.*, 1994; *Yin*, 2000; *DeCelles et al.*, 2002] (Figure 14). The single age on the timing of extension north of the Banggong suture zone is inconsistent with this model (Figure 14), although far more data on the timing of extension is needed in this region to systematically test this aspect of the model.

[33] *Cook and Royden* [2008], building on the work of *Royden* [1996], *Royden et al.* [1997], and *Shen et al.* [2001], developed a set of three-dimensional numerical models that investigated the effects of deformation of a laterally heterogeneous viscous crust on plateau growth. As applied to Tibet, models that incorporated a weak crustal region east of the Himalaya predicted shortening across the Himalaya and the Qilian Shan (northeast of the Qaidam Basin), EW extension across the center of the plateau, and clockwise rotation around the eastern Himalayan syntaxis. Based on these model results, *Cook and Royden* [2008] postulated that EW extension in the central plateau was driven by rapid flow of crustal material eastward into weak crust beneath the southeastern plateau. The initiation of uplift of the SE margin of the plateau at ~10 Ma [*Clark et al.*, 2005; *Ouimet et al.*, 2010] without significant shortening is similar to the timing of onset of accelerated EW extension on the plateau, suggesting that the proposed link between extension and uplift might be valid. As pointed out by *DeCelles et al.* [2007], little or no change in the high elevation across the plateau since at least the late Eocene to late Oligocene implies that eastward flow of middle or lower crust from beneath Tibet must have been balanced and partly driven by concurrent northward underthrusting of Indian crust beneath Tibet. Thus, two different, but linked processes operating in concert could have triggered onset of EW extension in northern and southern Tibet.

[34] Based on the similar timing of EW extension in Tibet, EW contraction across back-arc basins in eastern Asia, and development of new subduction zones in the western Pacific, *Yin* [2010] postulated that cessation of mantle upwelling and back-arc spreading along the eastern edge of Asia allowed the thickened Tibetan lithosphere to gravitationally spread toward the east. If the temporal link highlighted by *Yin* [2010] indicates true causality, eastward crustal flow from beneath Tibet, partly driven by underthrusting of Indian crust beneath Tibet, were likely contributing factors.

[35] In summary, the heterogeneous lithospheric structure across the plateau, absence of asthenosphere beneath Tibetan crust, and a little if any change in plateau elevation since at least the middle Miocene to late Eocene indicates that onset of extension is not correlative to increase in elevation and, therefore, the convective removal of mantle lithosphere hypothesis appears to be implausible. Constant stress mechanism models for driving extension also appear implausible because extension should be restricted to southern Tibet and hindered in central and northern Tibet. On the other hand, a combination of eastward flow of middle or lower crust from beneath Tibet accommodated by simultaneous northward underthrusting of Indian crust beneath Tibet appears to be a viable hypothesis because it can explain the onset of middle to late Miocene EW extension across the Himalayan orogeny from the high Himalaya to the Qiangtang Terrane. However, this model does not explain the apparent pulses of extension characterized by initiation of minor extension during the early Miocene with onset of slip along normal faults during the middle Miocene followed by a major pulse of accelerated normal slip during the middle to late Miocene. Clearly, far more data on the spatial and temporal distribution of normal faulting across the Tibetan Plateau, particularly within the Qiangtang Terrane, are needed to thoroughly characterize the processes that drove the onset of EW extension.

9. Conclusions

[36] Detailed new and published zircon and apatite (U-Th)/He thermochronometry, and inverse modeling of these ages from the footwall of the approximately NNW striking Kung Co normal fault yield insight into the timing of and slip rate along this fault. We suggest that subsequent to thermal reequilibration following emplacement of the ~19.1 Ma Kung Co granite, rapid fault slip along the Kung Co fault initiated at ~12–13 Ma, and downdip fault slip accelerated to an extreme rate of 21.9–6.9 mm/yr at ~10 Ma. This episode of footwall exhumation was followed by an episode of rapid thermal reequilibration that waned with time, and was followed by either quiescence or slow exhumation since ~9 Ma. Initiation and then acceleration of EW extension at 10–13 Ma along the Kung Co fault is similar to the onset of and acceleration of EW extension elsewhere across the south central part of the plateau, although this data set is relatively small. We suggest that a plausible explanation for the onset of EW extension across the Tibetan plateau was a combination of eastward flow of middle or lower crust from beneath Tibet accommodated and partly driven by simultaneous northward underthrusting of Indian crust beneath Tibet.

Appendix A

[37] In this section we briefly discuss the equations that are solved within the HeMP model and the parameters that go into the calculation of model ages. For a more detailed description of this method see *Ketcham et al.* [2000], *Ketcham* [2005], and *Flowers et al.* [2009].

[38] The time-temperature paths (t-T paths) are subdivided into discrete intervals following the rules that the individual interval cannot exceed a temperature range greater than 3.5°C and has to be shorter than 1% of the overall t-T path duration. This ensures accurate results while keeping computational time within reasonable limits.

[39] The first step in our calculation is the conversion of measured grain dimensions into spheres of equivalent radius

(a) using the surface-to-volume ratio (S/V) of the geometries of interest (tetragonal prism for zircon, hexagonal prism for apatite):

$$a = \frac{3}{S/V}$$

This transformation is supported by *Farley et al.* [1996] and *Meesters and Dunai* [2002], who showed that the effects of ^{4}He ejection due to long alpha stopping distances are proportional to the S/V of a variety of mineral geometries encountered in (U-Th)/He dating.

[40] The sphere is subsequently subdivided into a closely spaced grid (513 nodes) along its radius to track the He diffusion toward the periphery of the grain.

[41] To calculate a final model age for a given thermal history one has to keep track of how much daughter (^{4}He) is produced as well as how much ^{4}He is diffusing out of the grain during each interval. Because of the long stopping distances of ^{4}He particles traveling through the grain, an effective He production (A_{eff}) for each node has to be calculated to account for loss of ^{4}He due to ejection beyond the sphere radius. This is accomplished with following equation [see *Ketcham*, 2005]:

$$A_{eff,i,P} = \frac{\int_{X_i - S_p}^{X_i + S_p} A(X')dX}{\int_{X_i - S_p}^{X_i + S_p} dX}$$

where X_i is the radial position of the node, X' is the radial position of the shell edge relative to the spherical grain, S_P is the average stopping distance for parent isotope P (given in the work by *Farley et al.* [1996]), and A is the uncorrected He production. Using this in the general He generation equation:

$$^4He_i = 8A_{eff,i,238}\left(e^{\lambda_{238}t_2} - e^{\lambda_{238}t_1}\right) + 7A_{eff,i,235}\left(e^{\lambda_{235}t_2} - e^{\lambda_{235}t_1}\right) + 6A_{eff,i,232}\left(e^{\lambda_{232}t_2} - e^{\lambda_{232}t_1}\right) + 1A_{eff,i,147}\left(e^{\lambda_{147}t_2} - e^{\lambda_{147}t_1}\right)$$

we are then able to calculate the amount of ^{4}He produced at each node in the sphere during each interval bounded by t_1 and t_2. This quantity is added at the beginning of each interval and subsequently subject to diffusion for the duration of the interval at its mean temperature. As shown later, the solution for diffusion in a sphere contains the diffusivity that is traditionally calculated with the Arrhenius equation:

$$\frac{D}{a^2} = \frac{D_o}{a^2} * e^{-E/RT}$$

where D_o is the diffusivity at infinite temperature, E is the activation energy, R is the gas constant, and T is the mean temperature in Kelvin of the interval of interest. *Flowers et al.* [2009] derived an alternative calculation for the diffusivity of apatite that includes radiation damage as a function of effective uranium concentration in the equation. This Radiation-Damage-Accumulation-and-Annealing-Model (RDAAM) is implemented in our algorithm and applied to the modeled data set. Following *Flowers et al.* [2009], the diffusivity is calculated as

$$\frac{D}{a^2} = \frac{\frac{D_{oL}}{a^2} * e^{-E_L/RT}}{\left(k_o * v_{rd} * e^{E_{trap}/RT}\right) + 1}$$

where E_{trap} is the activation energy associated with the radiation damage traps; subscript "L" for diffusivity and activation energy is used to differentiate these quantities that were obtained from diffusion in undamaged crystals from the conventional notation values used in the conventional Arrhenius equation above; k_o is the radiation damage density scaled by v_{rd}.

[42] At this point we have converted the euhedral grain shapes into spheres of equivalent radii to reduce symmetry to a single dimension (radius) and defined the ejection corrected quantity of ^{4}He that needs to be added at each individual time interval along the t-T path. In the next step we utilize the Crank-Nicholson finite difference solution [e.g., *Press et al.*, 1988] to solve for diffusion in a sphere:

$$\frac{u_i^{n+1} - u_i^n}{\Delta t} = \frac{D}{2}\frac{\left(u_{i+1}^{n+1} - 2u_i^{n+1} + u_{i-1}^{n+1}\right) + \left(u_{i+1}^n - 2u_i^n + u_{i-1}^n\right)}{\Delta a^2} + A_{eff,i} * a$$

where u is the substitution of the He concentration multiplied by the radius, i subscript refers to the nodes along the radius, and n superscript to the interval number along the t-T path. Now we are able to track the amount of ^{4}He produced and diffused for each interval. Summing over the diffusion profile at present time given by the final ^{4}He concentration along the nodes and multiplying with the volume of the sphere gives the final amount of ^{4}He retained within the spherical geometry. Simply dividing this quantity by the He production rate yields the He model age:

$$\text{Age} = \left[^4He\right] / \left(8\lambda_{238}\,^{238}U + 7\lambda_{235}\,^{235}U + 6\lambda_{232}\,^{232}Th + 1\lambda_{147}\,^{147}Sm\right)$$

[43] To obtain a measure for the fit of the model age (τ_{mod}) compared to the actual sample age (τ_{meas}) we use the "goodness of fit (GOF)" criterion of *Ketcham et al.* [2000]:

$$GOF = 1 - \int_{\tau_{meas} - |\tau_{meas} - \tau_{mod}|}^{\tau_{meas} + |\tau_{meas} - \tau_{mod}|} \frac{1}{\sqrt{2\pi}} e^{-(x - \tau_{meas})^2 / 2\sigma_{meas}^2} dx$$

where σ refers to the uncertainty of the sample age. Based on the merit function of *Ketcham et al.* [2000], we define the model age as an acceptable solution if GOF > 0.05, and as a

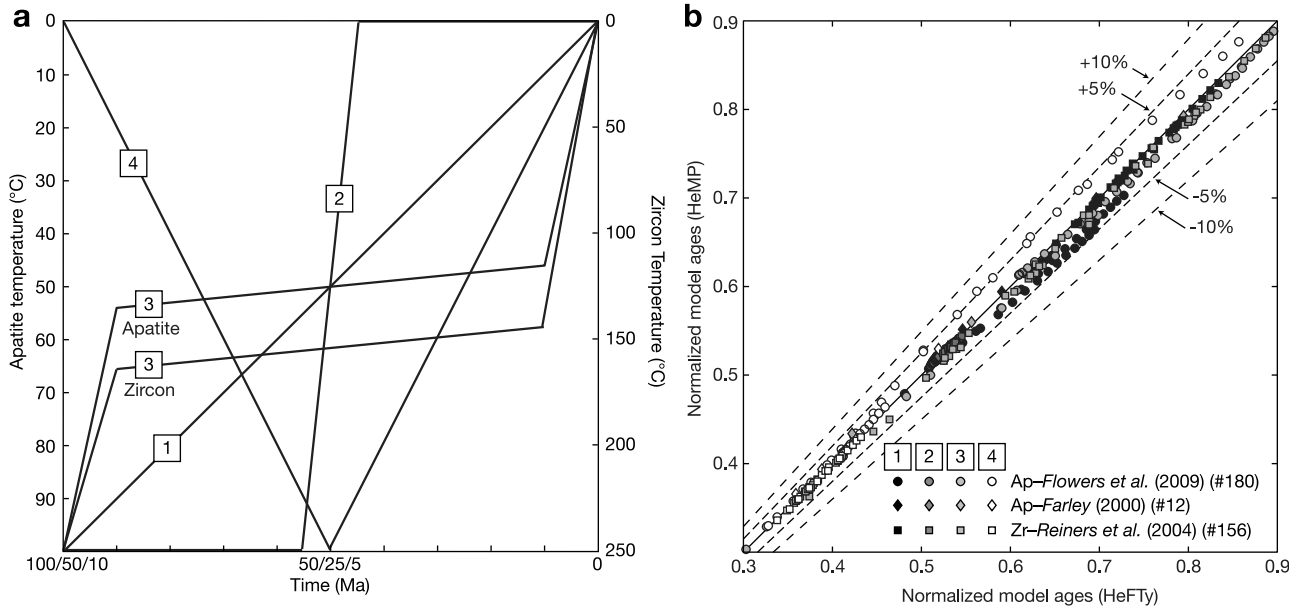

Figure A1. Test scenarios to compare HeFTy model ages [*Ketcham*, 2005] with results obtained from HeMP. (a) The four time-temperature evolutions used to evaluate the accuracy of our algorithm. Each time-temperature path was modeled for a duration of 100, 50, and 10 Myr to determine if our algorithm scales properly. (b) Normalized HeFTy model ages versus normalized HeMP model ages for a number of different apatite and zircon samples. Symbol fill corresponds to the time-temperature paths in Figure A1a; numeral indicates number of samples. Data from *Flowers et al.* [2009], *Farley* [2000], and *Reiners et al.* [2004].

good solution if GOF > 0.5. This value is calculated for each individual phase (apatite, zircon) for all the samples in the transect and only t-T paths that match all the sample ages (minus a user-defined number of allowed outliers) produce the statistically acceptable model ages shown in Figures 9 and 10. It is important to note that all the solutions are independent of each other and statistically equal, in other words, we do not use any technique to force the t-T paths in any direction once an acceptable fit was obtained but let the model explore all possible t-T combinations within the limits of the user constraints.

[44] To run these models, the user has to provide vertical sample spacing, grain dimensions, parent concentrations, and sample ages with uncertainties, all readily available from standard procedures in (U-Th)/He dating. For zircon, we used the diffusivity and activation energy from *Reiners* [2005], despite recent publications documenting anisotropic He diffusion behavior in zircon with respect to the c axis [*Cherniak et al.*, 2009]. *Wolfe and Stockli* [2010] demonstrated empirically, using a data set from the KTB ultradeep borehole, that bulk He diffusion parameters for zircons with commonly observed aspect ratios (1:3–1:5) adequately describe He diffusion behavior over geologic time. Furthermore, forward modeling of the well-established thermal history for the KTB, using bulk He diffusion parameters, produce an excellent fit with observed downhole zircon He data. Given the rapid cooling rate and the very short residence in the zircon He PRZ, any small differences in zircon He diffusion kinetics, related to diffusion anisotropy or radiation damage, are negligible as also demonstrated by *Wolfe and Stockli* [2010] and explored in our study. For these reasons, we feel that it is justified to use published bulk He diffusion behavior for this study as well.

[45] Due to the fact that we apply the RDAAM model from *Flowers et al.* [2009] to model apatite He ages, we are bound to use the diffusion kinetic and other parameters listed in their publication.

[46] Before we applied our approach to the discussed data set, in-depth testing against the HeFTy software was undertaken to ensure that our code is correct and can reproduce the results obtained from the above. A variety of synthetic apatite and zircon samples were forward modeled using four generic t-T histories (see Figure A1) that show (1) linear cooling, (2) very rapid cooling, (3) slow cooling through the He partial retention zone, and (4) linear reheating followed by linear cooling. Each of these t-T histories was modeled starting at t = 100, 50, and 10 Ma to check if our choice of interval lengths scales properly. As shown in Figure A1, the majority of the model ages are well within 5% of the results obtained from HeFTy, giving us the confidence that our model results are sufficiently accurate. A table showing all the results for each t-T history is available in Table S2.[1]

[1]Auxiliary materials are available in the HTML. doi:10.1029/2010TC002745.

[47] **Acknowledgments.** Discussions with W. Bohrson and F. Spera improved our understanding of magma cooling processes. Thanks to T. J. Dewane for completing the (U-Th)/He analyses and to G. Mahéo for providing latitude/longitude values for samples discussed by *Mahéo et al.* [2007]. Thorough and helpful comments from two anonymous reviewers, the Associate Editor A. Carter, and Editor T. Ehlers improved this manuscript. This study was financially supported in part by the grants-in-aid for Scientific Research grants 13573011 and 20403014 awarded to S. Wallis, National Science Foundation grants EAR-0309976 and EAR-0414817 awarded to D. Stockli, and Central Washington University. The Nordsim facility in Stockholm is operated under an agreement with the Joint Committee of the Nordic Research Councils for Natural Sciences; this is Nordsim contribution 282.

References

Armijo, R., P. Tapponnier, J. L. Mercier, and H. Tong-Lin (1986), Quaternary extension in southern Tibet: Field observations and tectonic implications, *J. Geophys. Res.*, *91*, 13,803–13,872, doi:10.1029/JB091iB14p13803.

Blisniuk, P. M., B. R. Hacker, J. Glodny, L. Ratschbacher, S. W. Bi, Z. H. Wu, M. O. McWilliams, and A. Calvert (2001), Normal faulting in central Tibet since at least 13.5 Myr ago, *Nature*, *412*, 628–632, doi:10.1038/35088045.

Cherniak, D. J., E. B. Watson, and J. B. Thomas (2009), Diffusion of helium in zircon and apatite, *Chem. Geol.*, *268*, 155–166, doi:10.1016/j.chemgeo.2009.08.011.

Clark, M. K., M. A. House, L. H. Royden, B. C. Burchfiel, K. X. Whipple, X. Zhang, and W. Tang (2005), Late Cenozoic uplift of southeastern Tibet, *Geology*, *33*, 525–528, doi:10.1130/G21265.1.

Coleman, M., and K. Hodges (1995), Evidence for Tibetan Plateau uplift before 14 Myr ago from a new minimum age for east-west extension, *Nature*, *374*, 49–52, doi:10.1038/374049a0.

Cook, K. L., and L. H. Royden (2008), The role of crustal strength variations in shaping orogenic plateaus, with application to Tibet, *J. Geophys. Res.*, *113*, B08407, doi:10.1029/2007JB005457.

Copley, A., and D. McKenzie (2007), Models of crustal flow in the India-Asia collision zone, *Geophys. J. Int.*, *169*, 683–698, doi:10.1111/j.1365-246X.2007.03343.x.

Cottle, J. M., M. J. Jessup, D. L. Newell, M. S. A. Horstwood, S. R. Noble, R. R. Parrish, D. J. Waters, and M. P. Searle (2009), Geochronology of granulitized eclogite from the Ama Drime Massif: Implications for the tectonic evolution of the South Tibetan Himalaya, *Tectonics*, *28*, TC1002, doi:10.1029/2008TC002256.

Currie, B. S., D. B. Rowley, and N. J. Tabor (2005), Mid-Miocene paleoaltimetry of southern Tibet: Implications for the role of mantle thickening and delamination in the Himalayan orogen, *Geology*, *33*, 181–184, doi:10.1130/G21170.1.

Cyr, A. J., B. S. Currie, and D. B. Rowley (2005), Geochemical evaluation of Fenghuoshan Group lacustrine carbonates, north-central Tibet: Implications for the paleoaltimetry of the Eocene Tibetan Plateau, *J. Geol.*, *113*, 517–533.

DeCelles, P. G., D. M. Robinson, and G. Zandt (2002), Implications of shortening in the Himalayan fold-thrust belt for uplift of the Tibetan Plateau, *Tectonics*, *21*(6), 1062, doi:10.1029/2001TC001322.

DeCelles, P. G., J. Quade, P. Kapp, M. Fan, D. L. Dettman, and L. Ding (2007), High and dry in the central Tibet during the Late Oligocene, *Earth Planet. Sci. Lett.*, *253*, 389–401, doi:10.1016/j.epsl.2006.11.001.

Dewane, T. J., D. F. Stockli, C. Hager, M. Taylor, L. Ding, J. Lee, and S. Wallis (2006), Timing of Cenozoic E-W extension in the Tangra Yum Co-Kung rift, south-central Tibet, *Eos Trans. AGU*, *87*(52), Fall Meet. Suppl., Abstract T34C-04.

Edwards, M. A., and T. M. Harrison (1997), When did the roof collapse? Late Miocene N-S extension in the High Himalaya revealed by Th-Pb dating of the Khula Kangri granite, *Geology*, *25*, 543–546, doi:10.1130/0091-7613(1997)025<0543:WDTRCL>2.3.CO;2.

Ehlers, T. A., and D. S. Chapman (1999), Normal fault thermal regimes: Conductive and hydrothermal heat transfer surrounding the Wasatch fault, Utah, *Tectonophysics*, *312*, 217–234, doi:10.1016/S0040-1951(99)00203-6.

Ehlers, T. A., and K. A. Farley (2003), Apatite (U-Th)/He thermochronometry: Methods and applications to problems in tectonic and surface process, *Earth Planet. Sci. Lett.*, *206*, 1–14, doi:10.1016/S0012-821X(02)01069-5.

Ehlers, T. A., P. A. Armstrong, and D. S. Chapman (2001), Normal fault thermal regimes and the interpretation of low-temperature thermochronometers, *Phys. Earth Planet. Inter.*, *126*, 179–194, doi:10.1016/S0031-9201(01)00254-0.

England, P., and G. Houseman (1989), Extension during continental convergence, with application to the Tibetan Plateau, *J. Geophys. Res.*, *94*, 17,561–17,579.

Farley, K. A. (2000), Helium diffusion from apatite: General behavior as illustrated by Durango fluorapatite, *J. Geophys. Res.*, *105*, 2903–2914.

Farley, K. A., R. A. Wolf, and L. T. Silver (1996), The effects of long alpha-stopping distances on (U-Th)/He ages, *Geochim. Cosmochim. Acta*, *60*, 4223–4229, doi:10.1016/S0016-7037(96)00193-7.

Fielding, E., B. Isacks, M. Barazangi, and C. Duncan (1994), How flat is Tibet?, *Geology*, *22*, 163–167, doi:10.1130/0091-7613(1994)022<0163:HFIT>2.3.CO;2.

Flowers, R. M., R. A. Ketcham, D. L. Shuster, and K. A. Farley (2009), Apatite (U-Th)/He thermochronometry using a radiation damage accumulation and annealing model, *Geochim. Cosmochim. Acta*, *73*, 2347–2365, doi:10.1016/j.gca.2009.01.015.

France-Lanord, C., S. M. F. Sheppard, and P. Le Fort (1988), Hydrogen and oxygen isotope variations in the High Himalaya peraluminous Manaslu leucogranite: Evidence for heterogeneous sedimentary source, *Geochim. Cosmochim. Acta*, *52*, 513–526, doi:10.1016/0016-7037(88)90107-X.

Garzione, C. N., D. L. Dettman, J. Quade, P. G. DeCelles, and R. F. Butler (2000a), High times on the Tibetan Plateau: Paleoelevation of the Thakkhola graben, Nepal, *Geology*, *28*, 339–342, doi:10.1130/0091-7613(2000)28<339:HTOTTP>2.0.CO;2.

Garzione, C. N., J. Quade, P. G. DeCelles, and N. B. English (2000b), Predicting paleoelevation of Tibet and the Himalaya from $\delta^{18}O$ vs. altitude gradients in meteoric water across the Nepal Himalaya, *Earth Planet. Sci. Lett.*, *183*, 215–229, doi:10.1016/S0012-821X(00)00252-1.

Garzione, C. N., P. G. DeCelles, D. G. Hodkinson, T. P. Ojha, and B. N. Upreti (2003), East-west extension and Miocene environmental change in the southern Tibetan Plateau; Thakkhola Graben, central Nepal, *Geol. Soc. Am. Bull.*, *115*, 3–20, doi:10.1130/0016-7606(2003)115<0003:EWEAME>2.0.CO;2.

Hager, C., and D. F. Stockli (2009), A new MATLAB©-based helium modeling package ("HeMP") for thermal history recovery from single and multi-thermochronometer (U-Th)/He data and data arrays, *Geol. Soc. Am. Abstr. Programs*, *41*, 487.

Hager, C., D. F. Stockli, T. J. Dewane, G. Gehrels, and L. Ding (2009), Anatomy and crustal evolution of the central Lhasa terrane (S-Tibet) revealed by investigations in the Xainza rift, *Geophys. Res. Abstr.*, *11*, EGU2009-11346-1.

Harrison, T. M., P. Copeland, W. S. F. Kidd, and A. Yin (1992), Raising Tibet, *Science*, *255*, 1663–1670, doi:10.1126/science.255.5052.1663.

Harrison, T. M., P. Copeland, W. S. F. Kidd, and O. M. Lovera (1995), Activation of the Nyainquentanghla Shear Zone: Implications for uplift of the southern Tibetan Plateau, *Tectonics*, *14*, 658–676, doi:10.1029/95TC00608.

Harrison, T. M., M. Grove, K. D. McKeegan, C. D. Coath, O. M. Lovera, and P. Le Fort (1999), Origin and episodic emplacement of the Manaslu intrusive complex, central Himalaya, *J. Petrol.*, *40*, 3–19.

Hintersberger, E., R. C. Thiede, M. R. Strecker, and B. R. Hacker (2010), East-west extension in the NW Indian Himalaya, *Geol. Soc. Am. Bull.*, *122*, 1499–1515, doi:10.1130/B26589.1.

Hirth, G., and J. Tullis (1992), Dislocation creep regimes in quartz aggregates, *J. Struct. Geol.*, *14*, 145–159, doi:10.1016/0191-8141(92)90053-Y.

House, M. A., K. A. Farley, and B. P. Kohn (1999), An empirical test of helium diffusion in apatite: Borehole data from the Otway Basin, Australia, *Earth Planet. Sci. Lett.*, *170*, 463–474, doi:10.1016/S0012-821X(99)00120-X.

Huang, W.-C., et al. (2000), Seismic polarization anisotropy beneath the central Tibetan Plateau, *J. Geophys. Res.*, *105*, 27,979–27,989, doi:10.1029/2000JB900339.

Jiménez-Munt, I., and J. P. Platt (2006), Influence of mantle dynamics on the topographic evolution of the Tibetan Plateau: Results from numerical modeling, *Tectonics*, *25*, TC6002, doi:10.1029/2006TC001963.

Kali, E., P. H. Leloup, N. Arnaud, G. Mahéo, D. Liu, E. Boutonnet, J. Van der Woerd, L. Xiaohan, J. Liu-Zeng, and L. Haibing (2010), Exhumation history of the deepest central Himalayan rocks (Ama Drime range): Key pressure-temperature-deformation-time constraints on orogenic models, *Tectonics*, *29*, TC2014, doi:10.1029/2009TC002551.

Kapp, P., and J. H. Guynn (2004), Indian punch rifts Tibet, *Geology*, *32*, 993–996, doi:10.1130/G20689.1.

Ketcham, R. A. (2005), Forward and inverse modeling of low-temperature thermochronometry data, *Rev. Mineral. Geochem.*, *58*, 275–314, doi:10.2138/rmg.2005.58.11.

Ketcham, R. A., R. A. Donelick, and M. B. Donelick (2000), AFTSolve: A program for multi-kinetic modeling of apatite fission-track data, *Geol. Mater. Res.*, *2*, 1–32.

Kind, R., et al. (2002), Seismic images of crust and upper mantle beneath Tibet: Evidence for Eurasian Plate subduction, *Science*, *298*, 1219–1221, doi:10.1126/science.1078115.

Klootwijk, C. T., P. J. Conaghan, and C. M. Powell (1985), The Himalayan arc: Large-scale continental subduction, oroclinal bending and back-arc spreading, *Earth Planet. Sci. Lett.*, *75*, 167–183, doi:10.1016/0012-821X(85)90099-8.

Kosarev, G., R. Kind, S. V. Sobolev, X. Yuan, W. Hanka, and S. Oreshin (1999), Seismic evidence for a detached Indian lithospheric mantle beneath Tibet, *Science*, *283*, 1306–1309, doi:10.1126/science.283.5406.1306.

Lee, J., and M. J. Whitehouse (2007), Onset of mid-crustal extensional flow in southern Tibet: Evidence from U/Pb zircon ages, *Geology*, *35*, 45–48, doi:10.1130/G22842A.1.

Lee, J., D. F. Stockli, L. A. Owen, R. C. Finkel, and R. Kislitsyn (2009), Exhumation of the Inyo Mountains, California: Implications for the timing of extension along the western boundary of the

Basin and Range Province and distribution of dextral fault slip rates across the eastern California shear zone, *Tectonics*, *28*, TC1001, doi:10.1029/2008TC002295.

Liu, M., and Y. Yang (2003), Extensional collapse of the Tibetan Plateau: Results of three-dimensional finite element modeling, *J. Geophys. Res.*, *108*(B8), 2361, doi:10.1029/2002JB002248.

Ludwig, K. R. (1998), On the treatment of concordant uranium-lead ages, *Geochim. Cosmochim. Acta*, *62*, 665–676, doi:10.1016/S0016-7037(98)00059-3.

Mahéo, G., P. H. Leloup, F. Valli, R. Lacassin, N. Arnaud, J.-L. Paquette, A. Fernandez, L. Haibing, K. A. Farley, and P.6 Tapponnier (2007), Post 4 Ma initiation of normal faulting in southern Tibet: Constraints from the Kung Co half graben, *Earth Planet. Sci. Lett.*, *256*, 233–243, doi:10.1016/j.epsl.2007.01.029.

Marrett, R., and R. W. Allmendinger (1990), Kinematic analysis of fault-slip data, *J. Struct. Geol.*, *12*, 973–986, doi:10.1016/0191-8141(90)90093-E.

McCaffrey, R., and J. Nabelek (1998), Role of oblique convergence in the active deformation of the Himalayas and southern Tibet plateau, *Geology*, *26*, 691–694, doi:10.1130/0091-7613(1998)026<0691:ROOCIT>2.3.CO;2.

McLaren, A. C., J. D. FitzGerald, and I. S. Williams (1994), The microstructure of zircon and its influence on the age determination from Pb/U isotopic ratios measured by ion microprobe, *Geochim. Cosmochim. Acta*, *58*, 993–1005, doi:10.1016/0016-7037(94)90521-5.

Meesters, A. G. C. A., and T. J. Dunai (2002), Solving the production-diffusion equation for finite diffusion domains of various shapes: Part l. Implications for low-temperature (U-Th)/He thermochronology, *Chem. Geol.*, *186*, 333–344, doi:10.1016/S0009-2541(01)00422-3.

Mercier, J.-L., R. Armijo, P. Tapponnier, E. Carey-Gailhardis, and H. T. Lin (1987), Change from late Tertiary compression to Quaternary extension in southern Tibet during the India-Asia collision, *Tectonics*, *6*, 275–304, doi:10.1029/TC006i003p00275.

Molnar, P. (2005), Mio-Pliocene growth of the Tibetan Plateau and evolution of East Asian climate, *Palaeontol. Electron.*, *8*, 1–23.

Molnar, P., and H. Lyon-Caen (1989), Fault plane solutions of earthquakes and active tectonics of the Tibetan Plateau and its margins, *Geophys. J. Int.*, *99*, 123–154.

Molnar, P., P. England, and J. Martinod (1993), Mantle dynamics, uplift of the Tibetan Plateau, and the Indian monsoon, *Rev. Geophys.*, *31*, 357–396, doi:10.1029/93RG02030.

Murphy, M. A., and P. Copeland (2005), Transtensional deformation in the central Himalaya and its role in accommodating growth of the Himalayan orogen, *Tectonics*, *24*, TC4012, doi:10.1029/2004TC001659.

Murphy, M. A., A. Yin, P. Kapp, T. M. Harrison, C. E. Manning, F. J. Ryerson, L. Ding, and J. Guo (2002), Structural evolution of the Gurla Mandhata detachment system, southwest Tibet: Implications for the eastward extent of the Karakoram fault system, *Geol. Soc. Am. Bull.*, *114*, 428–447, doi:10.1130/0016-7606(2002)114<0428:SEOTGM>2.0.CO;2.

Nabelek, J., et al. (2009), Underplating in the Himalaya-Tibet collision zone revealed by the Hi-CLIMB experiment, *Science*, *325*, 1371–1374, doi:10.1126/science.1167719.

Nelson, K. D., et al. (1996), Partially molten middle crust beneath southern Tibet: Synthesis of project INDEPTH results, *Science*, *274*, 1684–1688, doi:10.1126/science.274.5293.1684.

Ouimet, W., K. Whipple, L. Royden, P. Reiners, K. Hodges, and M. Pringle (2010), Regional incision of the eastern margin of the Tibetan Plateau, *Lithosphere*, *2*, 50–63, doi:10.1130/L57.1.

Owens, T. J., and G. Zandt (1997), Implications of crustal property variations for models of Tibetan plateau evolution, *Nature*, *387*, 37–43, doi:10.1038/387037a0.

Press, W. H., B. P. Flannery, S. A. Teukolsky, and W. T. Vetterling (1988), *Numerical Recipes in C—The Art of Scientific Computing, 993 pp., Cambridge Univ. Press, New York.*

Priestley, K., E. Debayle, D. McKenzie, and S. Pilidou (2006), Upper mantle structure of eastern Asia from multimode surface waveform tomography, *J. Geophys. Res.*, *111*, B10304, doi:10.1029/2005JB004082.

Priestley, K., J. Jackson, and D. McKenzie (2008), Lithospheric structure and deep earthquakes beneath India, the Himalaya and southern Tibet, *Geophys. J. Int.*, *172*, 345–362, doi:10.1111/j.1365-246X.2007.03636.x.

Pryer, L. L. (1993), Microstructures in feldspars from a major crustal thrust zone: The Grenville Front, Ontario, Canada, *J. Struct. Geol.*, *15*, 21–36, doi:10.1016/0191-8141(93)90076-M.

Reiners, P. W. (2005), Zircon (U-Th)/He thermochronometry, in *Low-Temperature Thermochronology: Techniques, Interpretations, and Applications*, edited by P. W. Reiners and T. A. Ehlers, pp. 151–179, Mineral. Soc. of Am., Chantilly, Va.

Reiners, P. W., T. L. Spell, S. Nicolescu, and K. A. Zanetti (2004), Zircon (U-Th)/He thermochronometry: He diffusion and comparisons with $^{40}Ar/^{39}Ar$ dating, *Geochim. Cosmochim. Acta*, *68*, 1857–1887.

Rodgers, A. J., and S. Y. Schwartz (1997), Low crustal velocities and mantle lithospheric variations in southern Tibet from regional Pnl waveforms, *Geophys. Res. Lett.*, *24*, 9–12, doi:10.1029/96GL03774.

Rodgers, A. J., and S. Y. Schwartz (1998), Lithospheric structure of the Qiangtang Terrane, northern Tibetan Plateau, from complete regional waveform modeling: Evidence for partial melt, *J. Geophys. Res.*, *103*, 7137–7152, doi:10.1029/97JB03535.

Rowley, D. B., and B. S. Currie (2006), Palaeo-altimetry of the late Eocene to Miocene Lunpola basin, central Tibet, *Nature*, *439*, 677–681, doi:10.1038/nature04506.

Rowley, D. B., and C. N. Garzione (2007), Stable isotope-based paleoaltimetry, *Annu. Rev. Earth Planet. Sci.*, *35*, 463–508, doi:10.1146/annurev.earth.35.031306.140155.

Rowley, D. B., R. T. Pierrehumbert, and B. S. Currie (2001), A new approach to stable isotope-based paleoaltimetry: Implications for paleoaltimetry and paleohypsometry of the High Himalaya since the late Miocene, *Earth Planet. Sci. Lett.*, *188*, 253–268, doi:10.1016/S0012-821X(01)00324-7.

Royden, L. (1996), Coupling and decoupling of crust and mantle in convergent orogens: Implications for strain partitioning in the crust, *J. Geophys. Res.*, *101*, 17,679–17,705, doi:10.1029/96JB00951.

Royden, L. H., B. C. Burchfiel, R. W. King, E. Wang, Z. Chen, F. Shen, and Y. Liu (1997), Surface deformation and lower crustal flow in eastern Tibet, *Science*, *276*, 788–790, doi:10.1126/science.276.5313.788.

Rubatto, D., and D. Gebauer (2000), Use of cathodoluminescence for U-Pb zircon dating by ion microprobe: Some examples from the western Alps, in *Cathodoluminescence in Geosciences*, edited by M. Pagel et al., pp. 373–400, Springer, Berlin.

Saylor, J. E., J. Quade, D. L. Dellman, P. G. DeCelles, P. A. Kapp, and L. Ding (2009), The late Miocene through present paleoelevation history of southwestern Tibet, *Am. J. Sci.*, *309*, 1–42, doi:10.2475/01.2009.01.

Saylor, J. E., P. G. DeCelles, and J. Quade (2010), Climate-driven environmental change in the Zhada basin, southwestern Tibet, *Geosphere*, *6*, 74–92, doi:10.1130/GES00507.1.

Shen, F., L. H. Royden, and B. C. Burchfiel (2001), Large-scale crustal deformation of the Tibetan Plateau, *J. Geophys. Res.*, *106*, 6793–6816, doi:10.1029/2000JB900389.

Shi, D., et al. (2004), Detection of southward intracontinental subduction of Tibetan lithosphere along the Bangong-Nujiang suture by P-to-S converted waves, *Geology*, *32*, 209–212, doi:10.1130/G19814.1.

Spicer, R. A., N. B. W. Harris, M. Widdowson, A. B. Herman, S. Guo, P. J. Valdes, J. A. Wolfek, and S. P. Kelley (2003), Constant elevation of southern Tibet over the past 15 million years, *Nature*, *421*, 622–624.

Stipp, M., H. Stünitz, R. Heilbronner, and S. M. Schmid (2002), The eastern Tonale fault zone: A "natural laboratory" for crystal plastic deformation of quartz over a temperature range from 250 to 700°C, *J. Struct. Geol.*, *24*, 1861–1884, doi:10.1016/S0191-8141(02)00035-4.

Stockli, D. F. (2005), Application of low-temperature thermochronology to extensional tectonic settings, in *Low-Temperature Thermochronology: Techniques, Interpretations, and Applications*, *Rev. Mineral. Geochem.*, vol. 58, edited by R. W. Reiners and T. A. Ehlers, pp. 411–448, Mineral. Soc. of Am., Chantilly, Va.

Stockli, D. F., K. A. Farley, and T. A. Dumitru (2000), Calibration of the apatite (U-Th)/He thermochronometer on an exhumed fault block, White Mountains, *Calif. Geol.*, *28*, 983–986.

Stockli, D. F., M. Taylor, A. Yin, T. M. Harrison, J. D'Andrea, P. Kapp, and L. Ding (2002), Late Miocene–Pliocene inception of E-W extension in Tibet as evidenced by apatite (U-Th)/He data, *Geol. Soc. Am. Abstr. Programs*, *34*, 411.

Tagami, T., K. A. Farley, and D. F. Stockli (2003), (U-Th)/He geochronology of single zircon grains of known Tertiary eruption age, *Earth Planet. Sci. Lett.*, *207*, 57–67, doi:10.1016/S0012-821X(02)01144-5.

Taylor, M., A. Yin, F. J. Ryerson, P. Kapp, and L. Ding (2003), Conjugate strike-slip faulting along the Bangong-Nujiang suture zone accommodates coeval east-west extension and north-south shortening in the interior of the Tibetan Plateau, *Tectonics*, *22*(4), 1044, doi:10.1029/2002TC001361.

Thiede, R. C., J. R. Arrowsmith, B. Bookhagen, M. McWilliams, E. R. Sobel, and M. R. Strecker (2006), Dome formation and extension in the Tethyan Himalaya, Leo Pargil, northwest India, *Geol. Soc. Am. Bull.*, *118*, 635–650, doi:10.1130/B25872.1.

Vavra, G., R. Schmid, and D. Gebauer (1999), Internal morphology, habit and U-Th-Pb microanalysis of amphibolite-to-granulite facies zircons: Geochronology of the Ivrea Zone (Southern Alps), *Contrib. Mineral. Petrol.*, *134*, 380–404, doi:10.1007/s004100050492.

Whittington, A. G., A. M. Hofmeister, and P. I. Nabelek (2009), Temperature-dependent thermal diffusivity of the Earth's crust and implications for magmatism, *Nature*, *458*, 319–321, doi:10.1038/nature07818.

Williams, H., S. Turner, S. Kelley, and N. Harris (2001), Age and composition of dikes in southern Tibet: New constraints on the timing of east-west extension and its relationship to postcollisional volcanism, *Geology*, *29*, 339–342, doi:10.1130/0091-7613(2001)029<0339:AACODI>2.0.CO;2.

Wolf, R. A., K. A. Farley, and L. T. Silver (1996), Helium diffusion and low temperature thermochronometry of apatite, *Geochim. Cosmochim. Acta*, *60*, 4231–4240, doi:10.1016/S0016-7037(96)00192-5.

Wolf, R. A., K. A. Farley, and D. M. Kass (1998), Modeling of the temperature sensitivity of the apatite (U-Th)/He thermochronometer, *Chem. Geol.*, *148*, 105–114, doi:10.1016/S0009-2541(98)00024-2.

Wolfe, M. R., and D. F. Stockli (2010), Zircon (U-Th)/He thermochronometry in the KTB drill hole, Germany, and its implications for bulk He diffusion kinetics in zircon, *Earth Planet. Sci. Lett.*, *295*, 69–82, doi:10.1016/j.epsl.2010.03.025.

Yin, A. (2000), Mode of Cenozoic east-west extension in Tibet suggesting a common origin of rifts in Asia during the Indo-Asian collision, *J. Geophys. Res.*, *105*, 21,745–21,759, doi:10.1029/2000JB900168.

Yin, A. (2010), Cenozoic tectonic evolution of Asia: A preliminary synthesis, *Tectonophysics*, *488*, 293–325.

Yin, A., T. M. Harrison, F. J. Ryerson, C. Wenji, W. S. F. Kidd, and P. Copeland (1994), Tertiary structural evolution of the Gangdese thrust system, southeastern Tibet, *J. Geophys. Res.*, *99*, 18,175–18,201, doi:10.1029/94JB00504.

Zhang, H., N. Harris, R. Parrish, S. Kelley, L. Zhang, N. Rogers, T. Argles, and J. King (2004), Causes and consequences of protracted melting of the mid-crust exposed in the North Himalayan antiform, *Earth Planet. Sci. Lett.*, *228*, 195–212, doi:10.1016/j.epsl.2004.09.031.

Zhang, P.-Z., et al. (2004), Continuous deformation of the Tibetan Plateau from global positioning system data, *Geology*, *32*, 809–812, doi:10.1130/G20554.1.

M. Aoya, Institute of Geology and Geoinformation, National Institute of Advanced Industrial Science and Technology, Central 7, Tsukuba 305-8567, Japan.

C. Hager, Chevron U.S.A. Inc., 1500 Louisiana St., Houston, TX 77002, USA.

J. Lee, Department of Geological Sciences, Central Washington University, Ellensburg, WA 98926, USA. (jeff@geology.cwu.edu)

D. F. Stockli, Department of Geology, University of Kansas, Lawrence, KS 66045, USA.

S. R. Wallis, Department of Earth and Planetary Sciences, Graduate School of Environmental Studies, Nagoya University, Nagoya 464-8602, Japan.

Y. Wang, Geologic Labs Center, China University of Geosciences, Beijing, 100083, China.

M. J. Whitehouse, Laboratory for Isotope Geology, Swedish Museum of Natural History, Box 50007, SE-104 05 Stockholm, Sweden.